We are IntechOpen, the world's leading publisher of Open Access books
Built by scientists, for scientists

4,800
Open access books available

122,000
International authors and editors

135M
Downloads

154
Countries delivered to

Our authors are among the

TOP 1%
most cited scientists

12.2%
Contributors from top 500 universities

CLARIVATE ANALYTICS
BOOK CITATION INDEX
INDEXED

WEB OF SCIENCE™

Selection of our books indexed in the Book Citation Index
in Web of Science™ Core Collection (BKCI)

Interested in publishing with us?
Contact book.department@intechopen.com

Numbers displayed above are based on latest data collected.
For more information visit www.intechopen.com

On the Fractography of Impact-Tested Samples of Al-Si Alloys for Automotive Alloys

Zheyuan Ma, Agnes M. Samuel,

Herbert W. Doty and Fawzy H. Samuel

Additional information is available at the end of the chapter

Abstract

Castings were prepared from both industrial and experimental 319.2, B319.2 and A356.2 alloy melts, containing Fe levels of 0.2–1.0 wt%. Stontium-modified (~200 ppm) melts were also prepared for each alloy/Fe level. Impact testing of heat-treated samples was carried out using an instrumented Charpy impact testing machine. At low Fe levels and high cooling rates (0.4% Fe, dendrite arm spacing (DAS) of 23 μm), crack initiation and propagation in unmodified 319 alloys occur through the cleavage of β-Al_5FeSi platelets (rather than by their decohesion from the matrix). The morphology of the platelets (individual or branched) is important in determining the direction of crack propagation. Cracks also propagate through the fracture of undissolved $CuAl_2$ or other Cu intermetallics, as well as through fragmented Si particles. In Sr-modified 319 alloys, cracks are mostly initiated by the fragmentation or cleavage of perforated β-phase platelets, in addition to that of coarse Si particles and undissolved Cu-intermetallics. In A356.2 alloys, cracks initiate mainly through the fracture of Si particles or their debonding from the Al matrix, while crack propagation occurs through the coalescence of fractured Si particles, except when β-Al_5FeSi intermetallics are present, in which case the latter takes precedence. In the Sr-modified case, cracks propagate through the linkage of fractured/debonded Si particles, as well as fragmented β-iron intermetallics. In samples exhibiting low-impact energies, crack initiation and propagation occur mainly through cleavage of the β-iron intermetallics.

Keywords: fracture mechanism, Al-Si alloys, impact testing, SEM, metallography

1. Introduction

Fractography is defined as the study and documentation of fracture surfaces [1]. The purpose of fractography is to analyze fracture features and attempt to relate the topography of the fracture surface to the causes and/or basic mechanisms of fracture. The knowledge of fracture behavior is important in upgrading material specifications, improving product design, and analyzing failures for improved reliability [2]. A study of the characteristics of fracture surfaces is often carried out using optical microscopy (viz., light-microscope fractography), particularly when a low magnification of the fracture surface is adequate. The magnification is usually selected such that a good resolution is obtained and can range from "macroscopic" or low magnification fields (up to 50 diameters) to "microscopic" or high magnification fields (50 diameters and above).

When very fine details of the fracture surface, e.g., dimples and microvoids, are required to be observed, a scanning electron microscope (viz., fractography) is used instead, where the magnifications can go from about 5 to 240,000 diameters. With a resolution limit of ~100 Å and a depth of field about 300 times that of an optical microscope, the SEM is generally preferred over the latter for the analysis of fracture surfaces.

Four major types of fracture (or failure) modes have been discussed in the literature. Briefly, these modes and the sources of their occurrence are as follows [3]:

1. Dimpled rupture (or microvoid coalescence) caused by ductile fracture or rapid overload fracture;

2. Cleavage or quasi-cleavage caused by brittle fracture or premature or overload failure by catastrophic rapid fracture;

3. Intergranular fracture caused by stress corrosion cracking, hydrogen embrittlement, or subcritical growth under sustained load; and

4. Ductile striations caused by fatigue cracking or subcritical growth under cyclic load.

The first three types are microstructurally dependent. Complications arise in determining the failure type when complex microstructures are involved. For example, in aluminum alloys containing extensive intermetallic compounds, the failure may occur by a combination of ductile rupture of the matrix and brittle cleavage of the intermetallic particles. Such intermetallic compounds (>1 μm) also reduce the alloy toughness. Often, transgranular fracture of the brittle compounds may also occur. Multiple microstructural phases can lead to numerous combinations of microscopic fracture modes.

Al-Si alloys are essentially a combination of the high strength, brittle silicon phase, and low-strength, ductile aluminum matrix containing, in addition, other microstructural features such as iron intermetallic phases, porosity, and inclusions. While it is natural to assume that the Si particles play an important role in the fracture behavior, the contribution of these other microstructural aspects must also be considered, even if their relative importance is affected by the amount and morphology of the constituents and the interactive effects between them.

Consequently, the alloying and melt-processing parameters (e.g., strontium modification, grain refining) and the solidification rates [different dendrite arm spacings (DASs)] which directly affect the microstructure also come into play.

Figure 1 shows two main types of fracture observed in the Al-Si alloy under tensile overloading. **Figure 1(a)** illustrates an example of the simple rupture mode of fracture, where the particles are observed at the bottom of the dimples. These particles are seen to have decohered from the surrounding matrix. In such cases, where decohesion of the particles takes place, the resultant fracture surface attains the dimpled appearance as seen in the figure. The alloy is said to have failed by the process of microvoid coalescence. The microvoids nucleate at regions of localized strain discontinuity, such as that associated with second-phase constituents, inclusions, grain boundaries, or dislocation pileups [4].
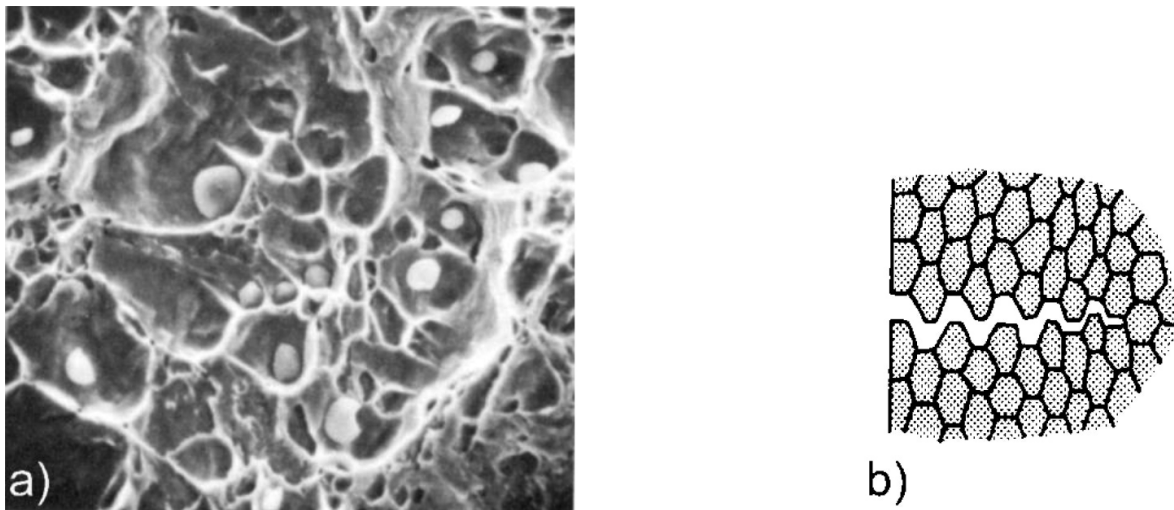
Figure 1. Two main types of fracture observed in Al-Si alloys under tensile overloading: (a) dimple rupture and (b) cleavage fracture of intermetallics [4].

Figure 1(b) represents an example of the cleavage fracture of intermetallics. Cleavage is a low-energy fracture that propagates along well-defined low-index crystallographic planes known as cleavage planes. Theoretically, a cleavage fracture should have perfectly matching faces and a completely flat and featureless surface. However, as the Al-Si alloys used are polycrystalline and contain grain boundaries, inclusions, and dislocations, these imperfections affect the propagating cleavage and alter the perfectly flat characteristics to a certain extent. Sometimes, the microconstituents present in the path of the propagating crack can result in the alloy sample exhibiting a mixed fracture mode, as was observed in the present study.

In this chapter, the fracture behavior of Al-Si-Cu and Al-Si-Mg cast alloys as reported by other researchers in the literature will be reviewed, to obtain a basic idea about the subject. Based on this, the fracture behavior of selected impact samples tested in the present study will be discussed. The focus is on alloy sample conditions corresponding to optimum or minimum impact energy conditions.

1.1. Si particles

Wang and Caceres [5] studied the fracture behavior of Al-Si-Mg (A356) alloys using tensile samples of different section sizes and under different conditions (as-cast/heat-treated, unmodified/Sr-modified), where *in situ* observations of the surface crack initiation and propagation using scanning electron microscopy (SEM) were presented. Cracks were found to initiate the fracture of Si particles at relatively low strain values. Crack propagation also proceeded by the same mechanism, preferably through the eutectic region of the microstructure, avoiding the primary Al dendrite cores wherever possible. Continued strain resulted in localized plastic deformation around the fractured Si particles, which eventually led to the formation of microcracks in the eutectic region. Further straining caused selected microcracks to link up with other neighboring microcracks in the same eutectic region to initiate the primary crack, or to link up with the propagating crack front. The overall fracture paths tended to follow the eutectic regions in the microstructure.

Ammar et al. [6] described the microstructure of A356 alloys consisting of primary Al-1% Si dendrites and a eutectic with silicon particles (12 pct volume) embedded in the Al-1% Si matrix. Room temperature constant amplitude fatigue tests revealed that for a low crack-tip driving force, the surface fatigue crack propagated primarily through the Al-1% Si dendrite cells. The silicon particles in the eutectic remained intact and served as barriers at low-fatigue crack propagation rates. When the fatigue crack crossed the three-dimensional Al-Si eutectic network, it propagated mainly along the interface between the silicon particles and the Al-1% Si matrix. Therefore, nearly all of the silicon particles were progressively debonded by fatigue cracks propagating at low rates, with the exception of elongated particles with a major axis perpendicular to the crack plane, which were fractured. For a high crack tip driving force, silicon particles ahead of the crack tip were fractured, and the crack subsequently propagated through the weakest distribution of prefractured particles in the Al-Si eutectic. Only small rounded silicon particles were observed to debond at high crack propagation rates. The crack process in the two cases is schematically depicted in **Figure 2**.
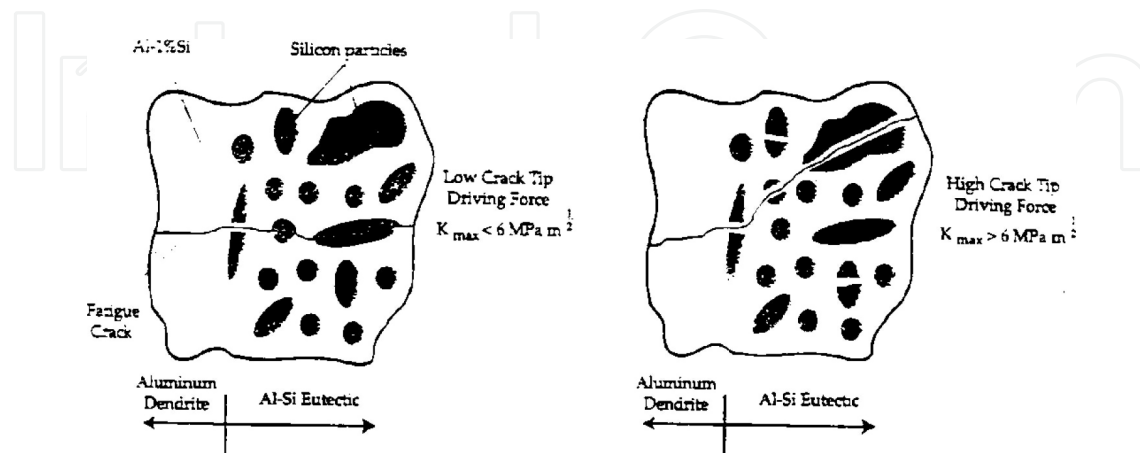
Figure 2. Schematic of the fatigue crack process through the silicon particle-rich eutectic regions at low and high crack-tip driving forces [7].

Hafiz and Kobayashi [8] conducted a study on the microstructure-fracture behavior relations in Al-Si casting alloys using tensile testing. The main focus was on Si particles, where different morphologies of the Si particles were obtained using a variety of solidification rates and different Sr levels. Fracture paths in the mid-sections were examined using optical microscopy, while the features of the fracture surface were examined using SEM. In general, the voids were found to initiate at silicon particles. The individual voids then grew and coalesced, creating microcracks in the eutectic region. These microcracks linked up to form the main crack, resulting in the final fracture.

Lee et al. [9] observed that the fatigue crack growth in Al-Si-Mg casting alloys occurs either by the nucleation and linkage of microcracks or voids formed as a result of the decohesion of non-fractured Si particles from the surrounding matrix (such as those encountered in modified alloys), or by cleavage or the cracking of silicon particles (such as those occurring in unmodified alloys), or both. In alloys containing intermediate Si particle size ranges, a mixed fracture morphology is observed, with both the cleavage fracture of Si particles and particle decohesion taking place.

Thus, the fracture mechanism proceeds as follows:

1. Cracking of the Si particles or their decohesion from the Al matrix at low strain;

2. Localized plastic deformation with increase in strain, leading to the formation of micro-cracks in eutectic regions;

3. Microcrack coalescence followed by crack propagation, leading to final fracture [3, 10].

Figure 3 shows a schematic representation of the process.
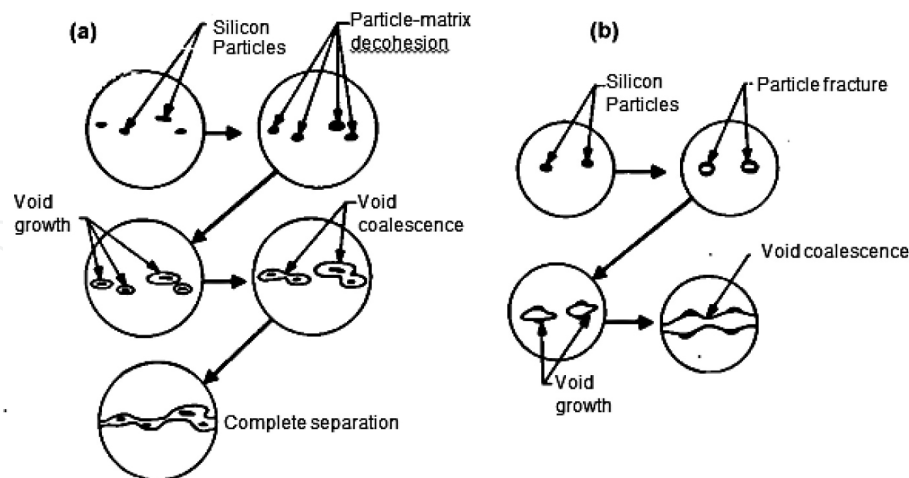

Figure 3. Schematic illustration of fracture mechanisms based on Si particles. (a) Initiation by Si particle-Al matrix interface decohesion and (b) initiation by Si particle fracture [11].

According to Ma et al. [3] in commercial A356 alloy, the fracture path of tensile-tested specimens proceeds mainly through the largest silicon particles, which constitute less than 1% of the overall population of silicon particles in the bulk microstructure. Li et al. [10] and Tirya-

kiolu [12] pointed out that the larger and longer silicon particles are more prone to cracking. In coarser structures, silicon particle cracking occurs at low strains, while in finer structures, the progression of damage is more gradual. They also found that in the former case, broken particles were observed at both cell and grain boundaries, with no evident preference for either, whereas in the case of finer structures, cracking is initiated on the grain boundaries. Lee et al. [9] also reported that the fatigue behavior of Al-Si-Mg casting alloys depends on the size, orientation, and local distribution of the Si particles.

1.2. Strontium modification

As strontium modification is commonly used to alter the morphology of the eutectic Si particles in Al-Si alloys, the process is expected to affect the fracture behavior of the alloy. Elsebaie et al. [13, 14] studied the role of microstructure in relation to the toughness of hypoeutectic Al-Si casting alloys, using unnotched Charpy impact test samples. Additions of 0.017 or 0.03 wt % Sr were used to modify the alloys. In the unmodified alloy, the fracture followed a path marked by the eutectic Si, circumventing the primary Al dendrites, where Si particles could be seen adhering to the sides of the crack path. The detection of submicron cracks showed that the fracturing of the Si particles corresponded to an early stage of the crack propagation process, i.e., the Si particles tended to fracture ahead of the main crack. In the modified alloy, the fracture propagated through both the eutectic region and the Al matrix, with sheared aluminum cells being detected in the fracture path, and the submicron cracks observed in the eutectic regions clearly indicated that the interdendritic structure had failed first.

Hafiz et al. [15] observed that in unmodified Al-8% Si alloy, the fracture surface mainly consists of a complicated array, resembling the Si array in the eutectic region containing cleaved Si particles. In addition, broken Si particles could also be detected. In the Sr-modified condition, two main features were observed: dimple colonies which represented the majority of the fracture surface and a smooth ripple pattern surrounding the dimple colonies, typical of ductile fracture.

According to several researchers [16–19], even though the fracture details are influenced by the Si particle morphology and the Al matrix, the basic fracture sequence is independent of changes in the microstructural characteristics due to the strontium modification. However, the addition of strontium does increase the amount of strain required to initiate and propagate the microcracks, particularly with respect to crack initiation.

1.3. Iron intermetallics

Their brittle nature, lateral or faceted growth mode (which makes them poorly bonded to the Al matrix) and the multiple (001) growth twins (parallel to the growth direction) of the plate-like β-Al$_5$FeSi iron intermetallic particles make them pro-crack sites. Hrong et al. [20] studied the fracture behavior of A356 alloys with different iron contents under resonant vibration. According to them, the cracks were found to initiate and grow along the eutectic Si- and Fe-rich intermetallic phase particles. The crack paths are propagated predominantly through the Si particles and occasionally through the Fe-rich intermetallics. When the iron content was

below 0.57 wt%, the iron intermetallics were mainly α-Al$_8$Mg$_3$FeSi$_6$ or α-Al$_5$Fe$_3$Si$_2$, whereas above that, the Fe-intermetallics occurred mostly as β-Al$_5$FeSi, which was found to be detrimental to the vibration fracture resistance.

According to Taylor [21], directly after the onset of plastic deformation, Al-7Si-0.3Mg sand-cast alloys display microcracks which are associated with brittle grain boundary cracking and cleavage of plate-shaped iron intermetallics, although the iron content is as low as 0.1 wt%. Intermetallics can be seen only in part of the grain boundaries that failed by brittle fracture. In die-cast alloys, microcracks occur due to fracture of small intermetallic particles located at interdendritic boundaries. With the increase in strain, Si particles at grain boundaries begin to fracture, followed by decohesion from the matrix.

Dinnis and Taylor [22] examined the microstructure of Al-7.0% Si-1.0% Fe alloys during tensile deformation using optical microscopy and *in situ* SEM. He found that the needle-like β-iron intermetallics are cracked easily in the earlier stages of deformation, whereas the α-iron Chinese script intermetallics can withstand a higher stress. When the form of the iron intermetallics was changed from Chinese script to needle-like, crack initiation did not occur at the silicon particles but at the iron intermetallics.

Villeneuve et al. [23] found that in Al-13% Si-Fe alloy castings, cracks appeared within the β-Al$_5$FeSi platelets rather than at the β/Al interface. This is due to the brittle nature of the β-phase, whereby the platelets are easily split into two halves.

1.4. Solidification rate

As the solidification rate directly affects the microstructure of an alloy casting, it is expected to affect the fracture behavior as well. The work of Alkahtani et al. [24] on the tensile testing of Al-7Si-0.3Mg alloy showed that, in sand-cast alloys, microcracks are associated with brittle grain boundary cracking and the cleavage of plate-shaped intermetallics and can be observed only in those parts of the grain boundaries that failed by brittle fracture, indicating an intergranular fracture mode. In die-cast alloys, all microcracks observed are due to the fracture of small intermetallic particles and located at interdendritic boundaries, indicating the fracture mode to be the transgranular type.

The work of Cáceres et al. [25] on fracture behavior of an Al-7Si-0.4Mg (A356.0) casting alloy shows that under low cooling rate conditions, when coarse structures are observed, the cell boundaries are distinct, the cracked particles are located with equal probability in the cell and grain boundaries, and the fracture mode is of the transgranular type. At high cooling rates (viz., in fine structures), the cracked particles are preferentially located in the grain boundaries, and the fracture mode is of the intergranular type.

In a similar study, Wang et al. [26] observed that in large cell-size materials, the fracture tends to occur along the dendritic cell boundaries (transgranular fracture), while for smaller cell-size materials, the fracture path runs along grain boundaries in an increasing proportion (intergranular fracture). The proportion of intergranular fracture increases from zero at large DAS values to about 60% for small DASs.

The work of Samuel and Samuel [27] on 319.2 alloys using end-chill castings showed that, in general, fracture surfaces of alloys obtained at 5-mm distance from the chill (DAS ~15 μm) displayed a transgranular mode of fracture, typical of ductile materials. At the highest distance from the chill (100 mm, DAS ~95 μm), however, the fracture was of the intergranular type, customarily associated with brittle, low-ductile materials.

1.5. Porosity

According to Dinnis et al. [28], after the onset of plastic deformation which generates micro-cracks, intense shear bands commonly form. They are oriented in directions of about 45 de-grees with respect to the tensile axis and propagate preferentially along grain boundaries. Microcracks grow and link along these shear bands. The presence of porosity can support shear band formation but does not initiate shear bands in the absence of the intermetallic particles. In certain cases, pores can even act as crack stoppers if located at the tips of sharp cracks.

Estensoro et al. [29] studied the fatigue behavior of two cast Al-7% Si alloys, with magnesium contents of 0.3 and 0.45%, respectively, and observed a very strong effect of defects (porosity) on the fatigue life. Fractographic examination showed that the strong scatter in fatigue life was associated with the amount of porosity in the specimen and determined by the number, size, and location of the pores in the fatigue specimens. The dispersion was more significant when the porosity emerged at the specimen surface. They also found that porosity exerts more influence on fatigue life than chemical composition or heat treatment.

In their investigation of the high-cycle fatigue testing of AlSi11 cast aluminum alloy, La-dos and Apelian [30] also showed that casting voids reduce the fatigue strength and lead to early fracturing. Crack initiation occurs at these voids, particularly if the porosity acts as a stress concentrator. The crack initiation times are strongly influenced by the position of the porosity, viz., whether it is close to the surface or to the center of the specimen. Savelli et al. [31] also reported that, in cast AlSi7Mg0.3 aluminum alloys, internal pores are responsible for the crack initiation of fatigue cracks. Based on this, a mathematical model was proposed by them to predict the fatigue life using pore dimensions as the main parameter.

2. Experimental procedure

The primary A356.2 and experimental 319 alloys used in this study were supplied in the form of 12.5-kg ingots. The chemical compositions of the as-received alloys are listed in **Table 1**. The two 319 alloys used differ from each other in their Mg contents, where the B319.2 alloy contained 0.4 wt% Mg compared to 0.002 wt% in the 319.2 alloy. The Mg level of 319 alloys used in automotive applications is generally of the order of ~0.4 wt%.

Study code	AA alloy	Element (wt%)									
		Si	Cu	Mg	Fe	Mn	Zn	Ti	Sr	Pb	Al
EA	319.2	6.06	2.98	0.002	0.12	0.023	0.006	0.007	0.0003	–	bal.
IA	319.2	6.12	3.57	0.0719	0.405	0.0939	0.0483	0.138	0.00024	–	bal.
IB*	B319.2	6.22	3.21	0.40	0.15	0.026	0.0034	0.0075	–	–	bal.
IC	A356.2	6.78	0.02	0.33	0.11	0.04	0.04	0.08	–	0.03	bal.

*IB alloy was prepared from EA alloy where the Mg level was increased to 0.4 wt%.

Table 1. Chemical compositions of 319 and 356 alloys.

Fracture surfaces of impact-tested samples were examined in order to determine the crack initiation and propagation behavior with respect to the alloy compositions and melt treatment conditions. Samples were cut approximately a quarter inch from the fracture surface where the upper part was used for examination. Extra care was taken during the cutting to avoid contamination of the fracture surface. The bottom of the sample was ground to flatten it and then mounted on a standard base with a special glue. Several samples were kept together in a box and classified systematically according to their chemical compositions and melt treatment conditions before they were placed into the specimen chamber of a scanning electron microscope. The SEM work was carried out using a scanning electron microscope operating at 15 kV.

3. Fractography results

Optical microscopy and SEM were used to examine the facture surfaces of selected impact-tested samples. In each alloy, samples with the lowest and highest iron levels were taken, obtained at the highest and lowest cooling rates (i.e., at DASs of ~23 and ~85 μm). In each case, at least two SEM micrographs were taken, one from the edge and one from the central region of the fracture surface, to observe the crack initiation and crack propagation characteristics, respectively. In addition, interesting features appearing on the fracture surface were also examined. Optical micrographs from longitudinal sections (perpendicular to the fracture surface) of these samples, particularly those of A356.2 alloy, were also obtained, to further interpret the fracture process.

3.1. SEM fractography

The popular use of a scanning electron microscope for fractography studies is on account of the fact that it allows for a direct examination of the fracture surface without the need for a replica, as in the case of transmission electron microscopy. One of the great advantages of the SEM is its ability to examine specimens at low magnifications of about 50 diameters and then enlarge regions of special interest to very high magnifications.

Both backscattered electron and secondary electron modes of operation are normally used for fractographic purposes. The secondary electron image (SEI) offers a better resolution, whereas

the backscattered electron image (BEI) offers an improved image contrast that is necessary in the case of smooth specimens and at low magnifications. The high image contrast is, however, accompanied by a loss of resolution, inherent with the backscattered mode of operation.

Backscattered electrons are electrons with high energy (equivalent to that provided by the accelerating voltage, which is usually in the range of 20–25 kV). The electrons escape from as deep as 300 Å in the specimen. Because of scatter within the specimen, the resultant source is much larger in diameter than the incident-beam diameter. On the contrary, the secondary electrons that are generated possess energies of about 20–50 eV (maximum), which is no more than is required for the electrons to escape from the top 100 Å layer of the specimen. A zone within 100 Å of the surface, then, constitutes the source of secondary electrons that can be captured by the electron collectors. Secondary electrons generated further within the specimen do not have enough energy to escape. The difference in the volume of the source for the two types of electrons accounts for the difference in resolution [32]. Most of the fractographs presented here are BEIs, to bring out the contrast in the various features observed on the fracture surfaces of the samples studied.

3.2. Alloys 319.2 and B319.2 (alloys A and B)

The SEM fractographs of the 319.2 alloy sample corresponding to the 0.4% iron level and highest cooling rate are presented in **Figures 4** and **5**, taken respectively from the sample edge where the sample was hit during impact testing and the center of the sample surface.
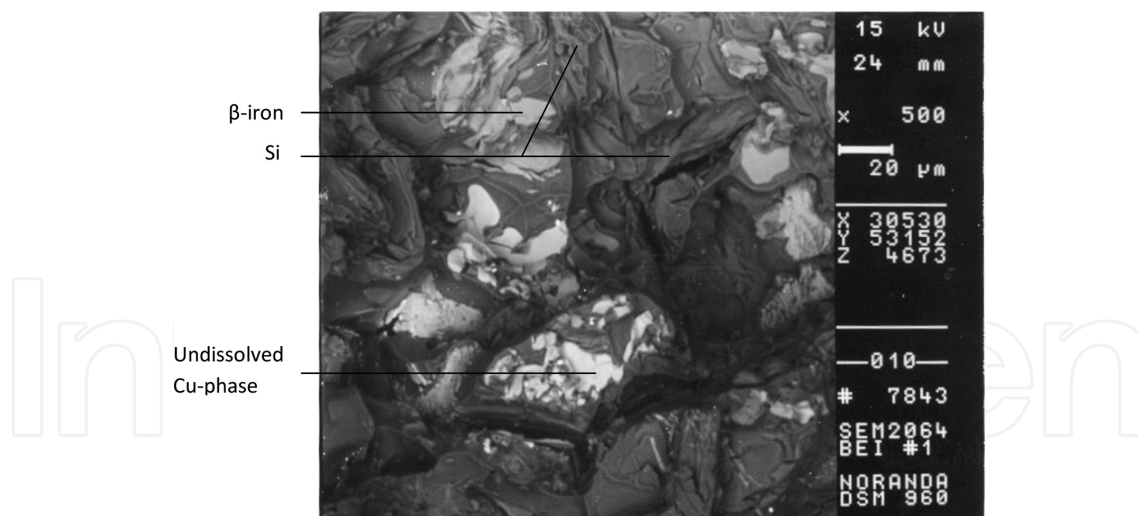
Figure 4. SEM micrograph showing fracture surface of alloy 319.2 (0.4% Fe, DAS 23 μm, unmodified, edge).

The features exhibited in **Figure 4** are typical of cleavage fracture, as is expected to be the case at high deformation rates during impact loading. The fracture plane changes orientation from grain to grain. A certain amount of intergranular cleavage is also observed in the form of secondary cracks. The fracture surface reveals the presence of β-Al_5FeSi iron intermetallic platelets, undissolved $CuAl_2$ or Al_7Cu_2Fe (insoluble phase) particles (since all alloy samples

were T6-heat treated), and acicular Si particles surrounding them. The fragmentation of all three particle types indicates that possibly all three could have acted as crack initiation sites. The microstructural constituents of interest in **Figure 4** and those that follow have been marked in each case.

Figure 5, taken from the central region of the fracture surface of the same sample, shows a cracked α-iron script particle, surrounded by brighter Cu-containing phase particles on either side. The presence of cracks within these particles confirms how crack formation is facilitated when such intermetallics are present in the microstructure.
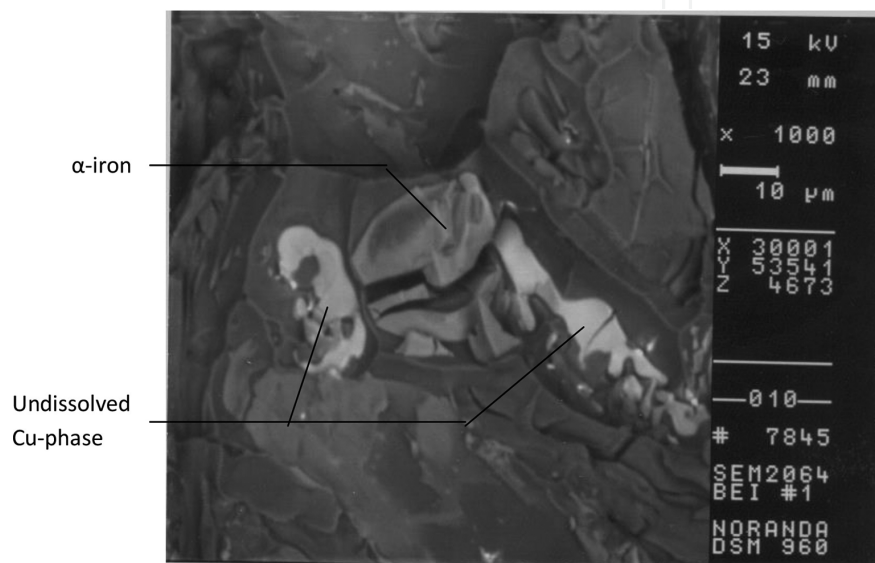
Figure 5. SEM micrograph showing fracture surface of alloy 319.2 (0.4% Fe, DAS 23 μm, unmodified, center).

At the highest iron level (0.8%) and lowest cooling rate, the SEM fractograph of **Figure 6** reveals that crack initiation occurs by massive cleavage of the brittle β-Al$_5$FeSi phase. A profusion of β-platelets is expected to be observed in the alloy microstructure at such Fe levels and, as can be seen, the crack propagates from one β-platelet across the other, along the direction delineated by the open arrows. In an ordinary two-dimensional optical micrograph, these β-platelets would appear in the form of branched needles. The much larger dimensions of the plate-like β-Al$_5$FeSi phase would make it more susceptible to crack initiation compared to the Si particles, even if the latter occurs in brittle, acicular form in the unmodified alloy.

In cleavage fracture, the fracture path follows a transgranular plane that is usually a well-defined crystallographic plane, as is judged to be the case by the relatively smooth surfaces of the β-platelets seen in **Figure 6**. The central area of the fracture surface of the same sample, **Figure 7**, shows instances of the Cu-containing (brighter) phase, precipitated on the β-platelets, amplifying the likelihood for crack propagation through these locations. The crack propagates in the direction denoted by the open arrows, along the cleaved intermetallic particles. A number of secondary cracks are also observed in the vicinity. In keeping with the brittle fracture features observed in **Figures 6** and **7**, this sample exhibited a low impact energy of 1.90 J.

In the case of the modified 319.2 alloy containing 0.4% Fe and obtained at the highest cooling rate, the SEM fractographs, **Figures 8** and **9**, revealed considerably different characteristics. Upon application of a high deformation rate during impact loading, **Figure 8**, the β-platelet at the edge of the sample fragmented into several smaller segments, rather than undergoing cleavage as was observed in **Figure 4** for the unmodified alloy. Keeping in mind the effect of Sr (in the modified alloy) on the dissolution and fragmentation of the β-Al₅FeSi phase, the
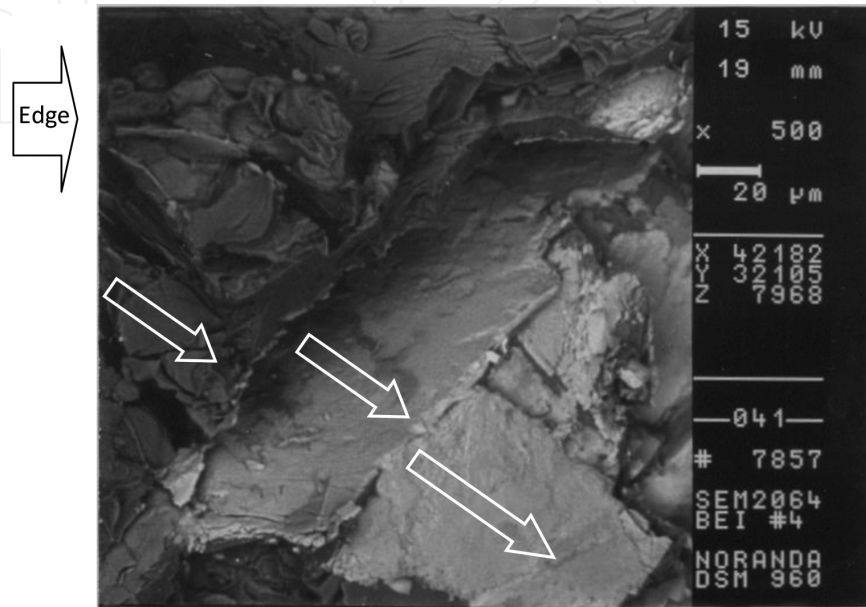
Figure 6. SEM micrograph showing fracture surface of alloy 319.2 (0.8% Fe, DAS 83 μm, unmodified, edge).
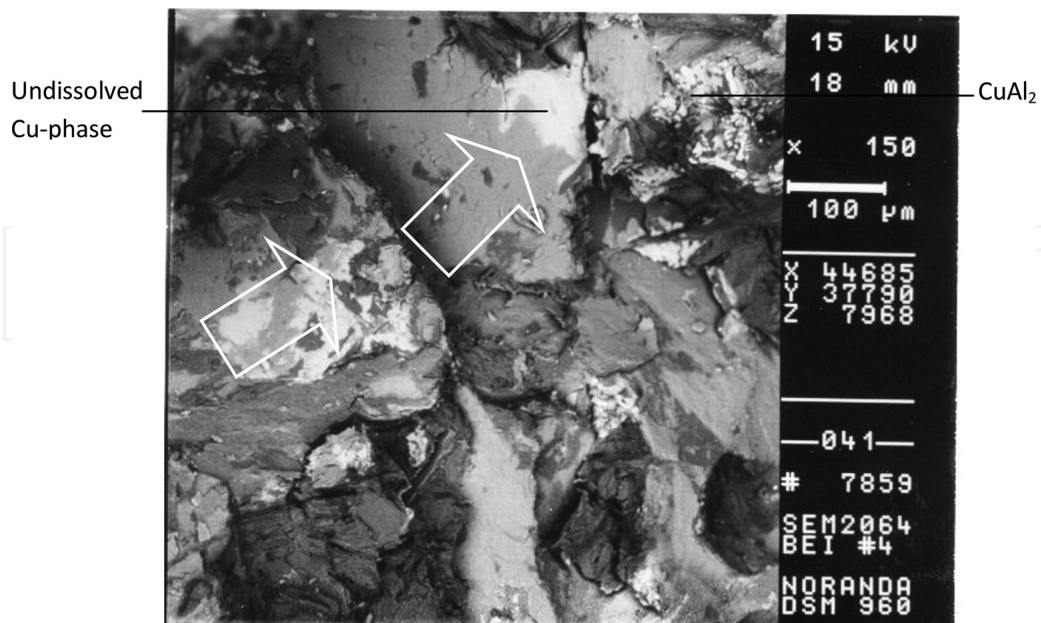
Figure 7. SEM micrograph showing fracture surface of alloy 319.2 (0.8% Fe, DAS 83 μm, unmodified, center).

deterioration of the β-phase caused by Sr addition would more likely result in the fragmentation of the β-platelets rather than their cleavage (as observed in the case of solid β-platelets in the unmodified alloy). Consequently, crack propagation would proceed at a slower rate, leading to higher impact energy, as indicated by the E_I, E_P, and E_T values of 16.39, 14.57, and 30.96 J, respectively. In addition, the transformation of the eutectic Si particles from acicular to fibrous form would also result in a more ductile fracture mode.
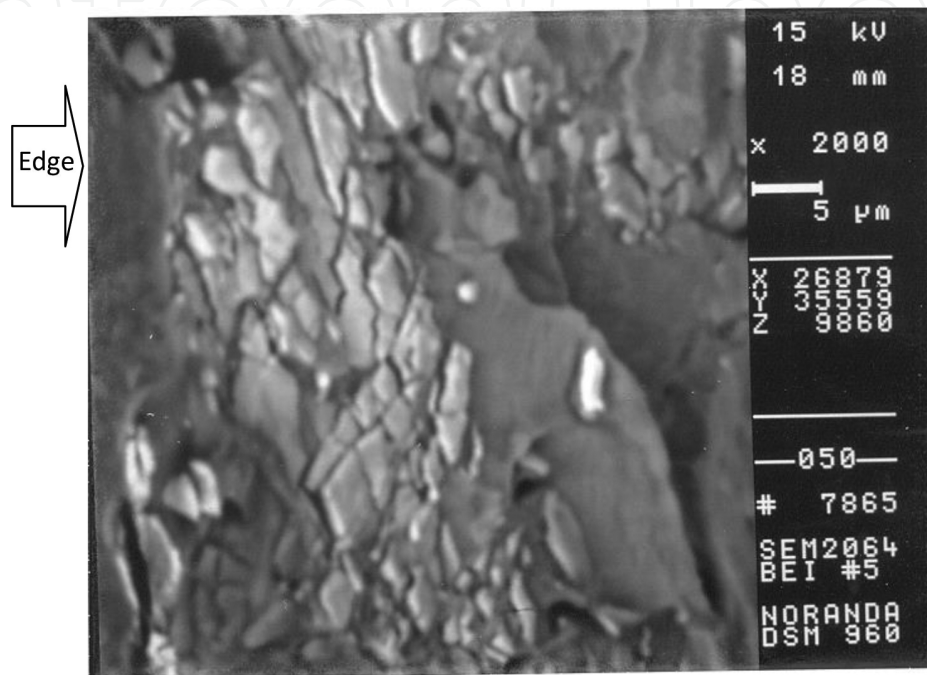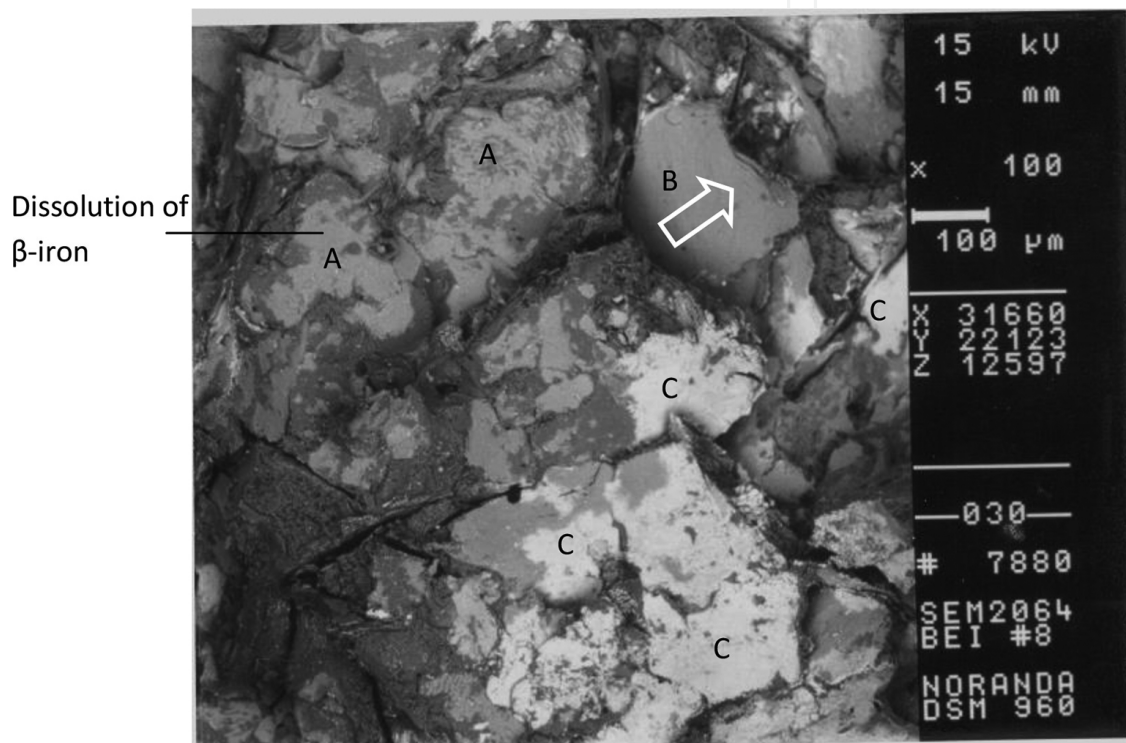

Figure 8. SEM micrograph showing fracture surface of alloy 319.2 (0.4% Fe, DAS 23 μm, modified, edge).
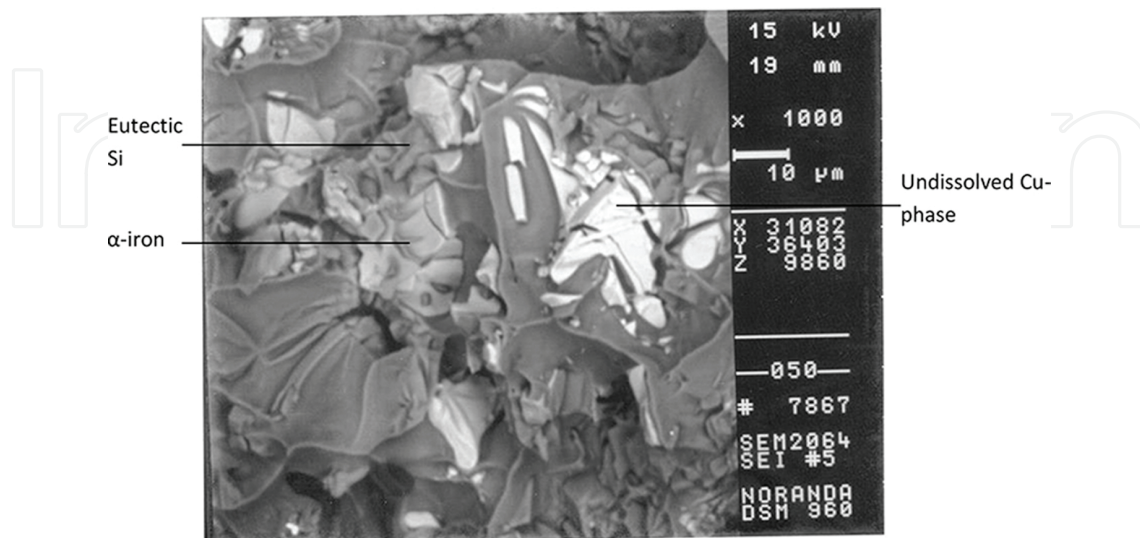
Figure 9. SEM micrograph showing fracture surface of alloy 319.2 (0.4% Fe, DAS 23 μm, modified, center).

Comparing the much higher magnification image of **Figure 8** (2000X) with that of **Figure 4** (500X), one may also estimate the much smaller sizes of the β-platelets obtained in the modified alloy. **Figure 9** shows fractured α-iron script and Cu-containing phase (bright) particles. Due to the surrounding eutectic structure, the fracture surface is more reminiscent of ductile, rather than brittle fracture, in spite of the cracks observed in the $CuAl_2$ particles.

In summary, therefore, Sr-modified Fe-containing 319.2 alloys would be expected to exhibit a mixed fracture mode. This is also reflected by their increased ductility, as was observed from the tensile test results.
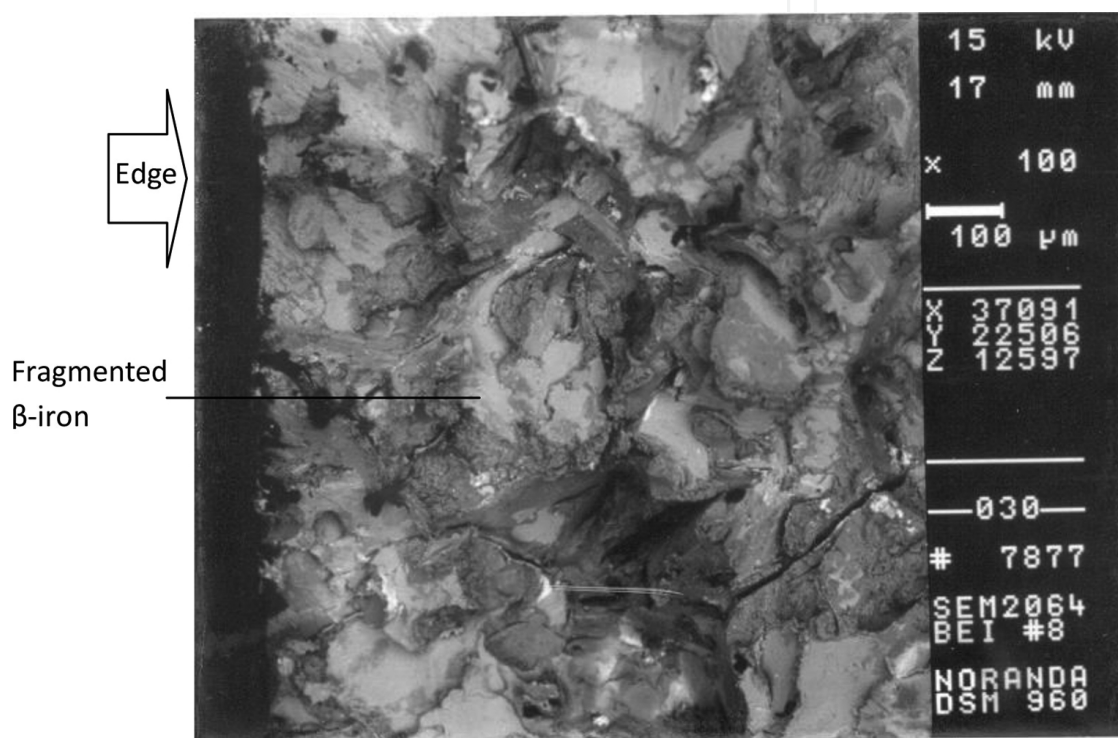
Figure 10. SEM micrograph showing fracture surface of alloy 319.2 (0.8% Fe, DAS 83 μm, modified, edge).

Figures 10 and **11** show SEM fractographs taken from the modified 319.2 alloy sample containing 0.8% Fe and obtained at the lowest cooling rate. Comparing **Figure 10** with **Figure 6** corresponding to the same alloy in the unmodified condition, the effect of Sr on the β-Al_5FeSi phase is evidenced, in the deteriorated appearance of the latter (see medium gray regions all over the fracture surface). The small bright spots in **Figure 10** correspond to particles of undissolved $CuAl_2$. In **Figure 11**, however, the bright regions (marked C) viewed on top of the β-platelets are Cu-containing phases, most likely Al_7Cu_2Fe. As observed by Li et al. [10, 33], this phase is insoluble even after 100 h solution heat treatment at 500°C. Compared to the flat surface of the β-platelet marked B, the perforated nature of those marked A is quite clear. Due to the high Fe content of the alloy, the volume fraction of β-Al_5FeSi phase, although considerable, appears distributed as smaller platelets all over the microstructure. It is interesting to note from the smooth surface of the β-platelet at B (and that at C below) that the β-platelets

not modified by Sr cracked by cleavage quite easily, whereas elsewhere, the crack passed through other regions (e.g., eutectic Si) as well, as evidenced by the intergranular cracking.

Both cleavage fracture and intergranular fracture are characteristically low-energy mechanisms, and the simultaneous operation of both can occur when the resolved stresses for transgranular cleavage are approximately equal. Also, if the preferred grain boundary fracture path is not continuous, and if the cleavage stress is relatively low, the regions that do not fracture intergranularly can fracture by cleavage. **Figure 11** shows an example of this type of fracture.

Figure 11. SEM micrograph showing fracture surface of alloy 319.2 (0.8% Fe, DAS 83 μm, modified, center).

From the overall mode of fracture observed in **Figures 10** and **11**, the modified alloy exhibits more resistance to crack propagation than that offered by the unmodified alloy (cf. E_I and E_P of 1.30 and 0.60 J with 1.63 and 1.43 J in the unmodified and modified alloys, respectively) where the brittle fracture/cleave features reflect the ease of crack propagation in that sample.

In what follows, some of the interesting features that were observed in the analysis of the fracture surfaces of various 319.2 alloy samples studied will be shown. These samples were selected to highlight other microstructural aspects such as inclusions or porosity, besides the α- and β-iron intermetallics and Si particles, which could affect the fracture behavior.

The SEM micrograph of **Figure 12** shows the cleavage fracture of an α-AlFeSi intermetallic particle in the modified 319.2 alloy sample containing 0.8% Fe and obtained at the highest cooling rate. The fracture consists of several cleavage steps that provide an indication of the

local direction of crack growth. Further above, the cleavage planes followed by the crack show various alignments, as influenced by the orientations of individual grains.

Another feature of cleavage fracture, the "tongue" appears on cleavage facets as very fine slivers (see arrows marked T) that result from cleavage across micro-turns formed by plastic deformation at the tip of the main propagating crack. Around the α-AlFeSi particle, the surrounding eutectic Si regions are identified by the small microvoids and dimpled nature of the fracture surface, indicating the mixed fracture mode of the sample. The E_I, E_P, and E_T in this case are 8.71, 1.31, and 10.02 J, respectively.
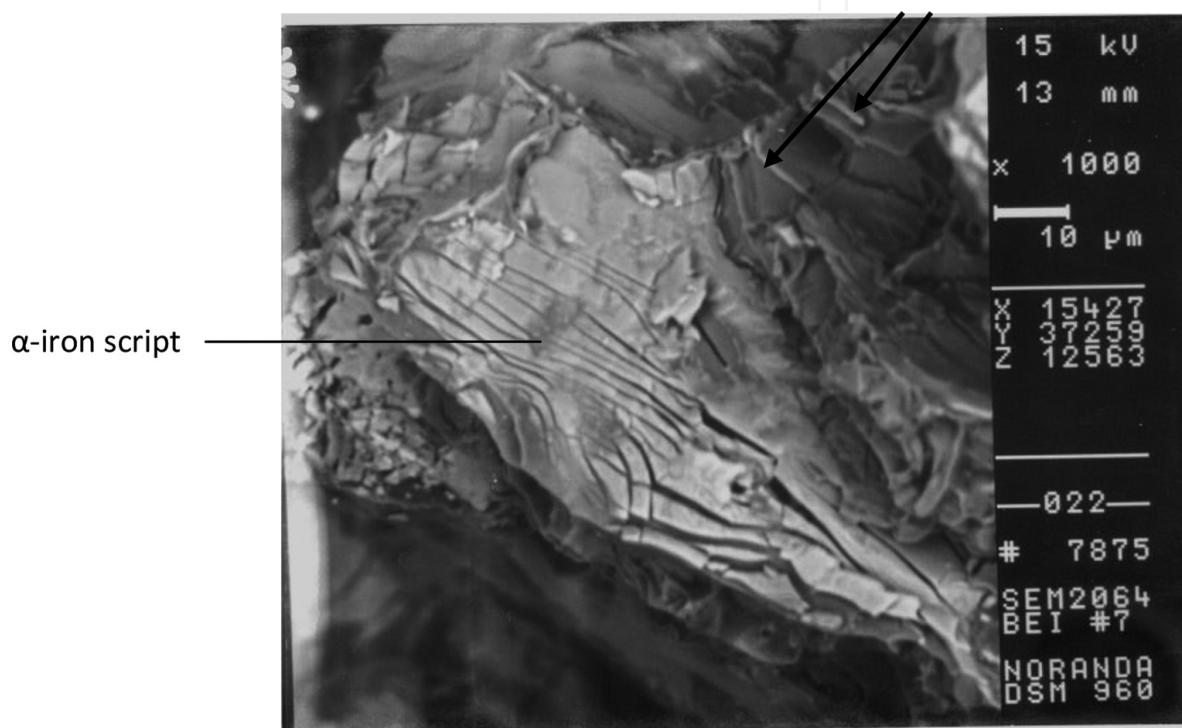
Figure 12. SEM micrograph showing fracture of α-AlFeSi intermetallics in alloy 319.2 (0.8% Fe, DAS 23 μm, modified).

It should be mentioned here that the iron intermetallic phases/particles referred to in the different fractographs presented in this chapter were identified using EDS analysis. The flat cleaved surfaces of these iron intermetallics facilitated identification. For the Cu-containing particles, it was difficult to obtain the exact composition of the $CuAl_2$ particles due to their size and the uneven nature of the surrounding fracture surface. In the case of the Al_7Cu_2Fe phase, as it occurred on top of the β-Al_5FeSi phase (the precipitation of the Al_7Cu_2Fe phase follows that of the β-Al_5FeSi phase [34]), its composition could not be verified correctly, as well.

Figure 13 shows another fractograph of the same sample, where the fracture surface consists of interlinked β-phase regions that would probably correspond to more than one branched β-platelets. Alpha-Al dendrites appear through parts of the β-phase where dissolution of the platelets has occurred. Dimpled rupture of the eutectic Si regions interspersed in between is also observed. The shallow, depressed nature of the dendrite observed near the white arrow,

together with the darker void region below (black arrow), indicate the existence of a pore in this area, which would have facilitated crack propagation. The smooth interface between the β-phase and the α-Al dendrite and the pore linked to them affirms the feedability-related characteristics of the β-platelet phase, aiding in the formation of porosity.
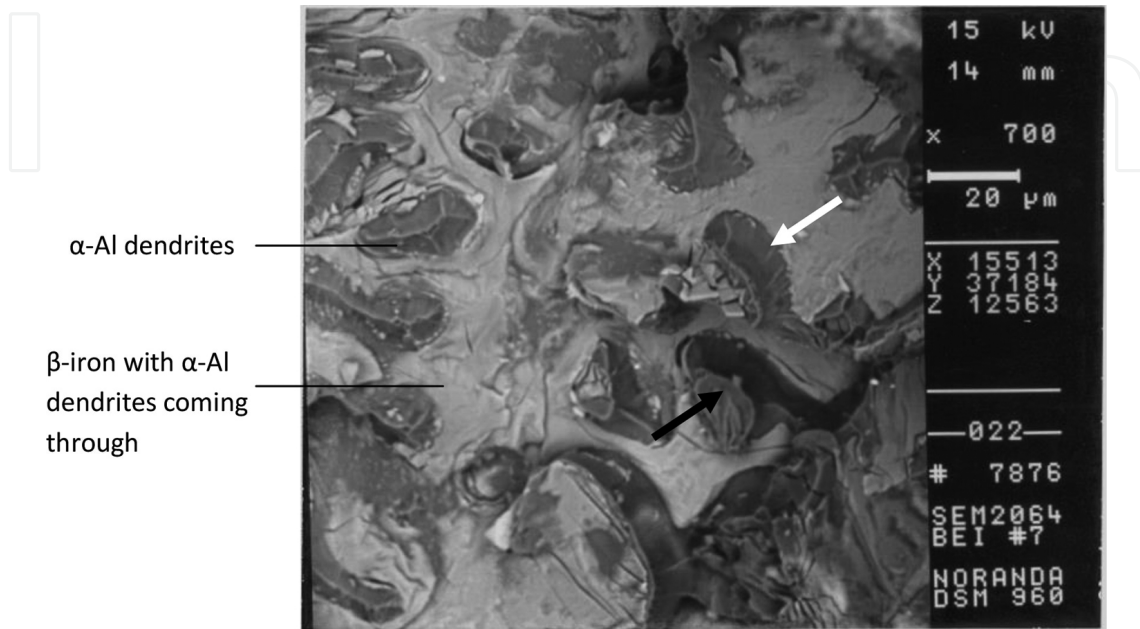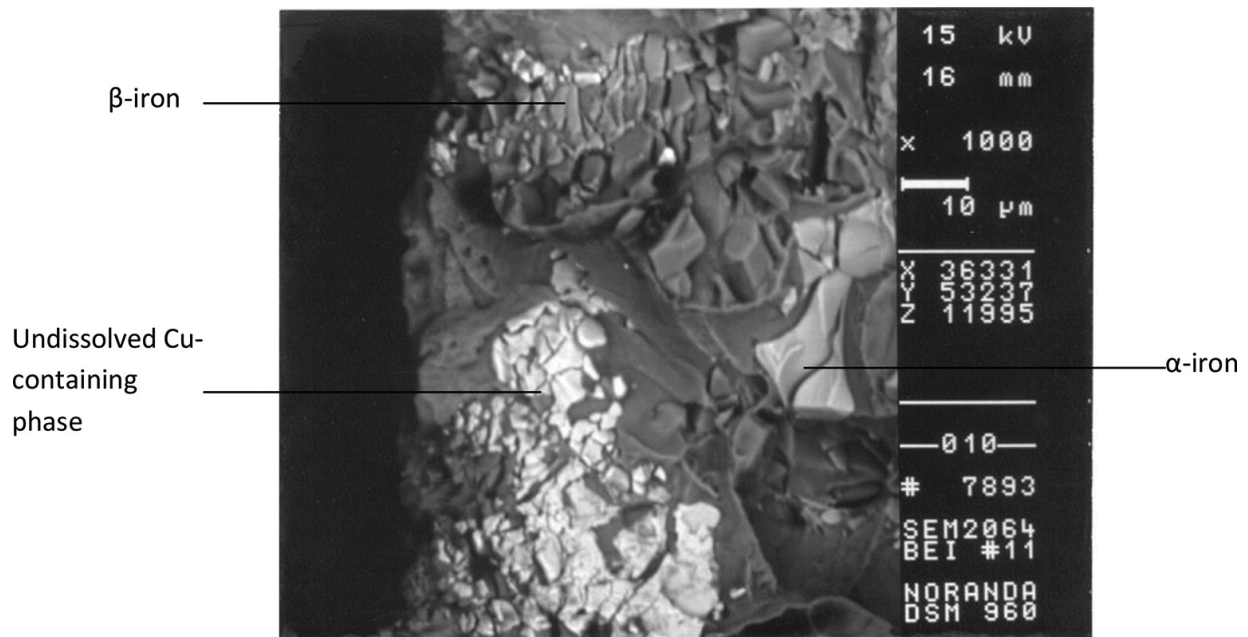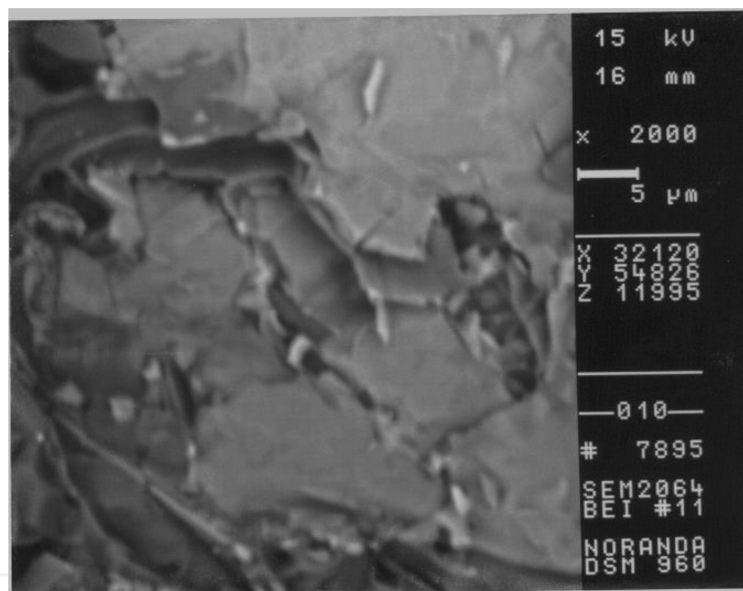

Figure 13. SEM micrograph showing fracture of β-AlFeSi intermetallics in alloy 319.2 (0.8% Fe, DAS 23 μm, modified).

Figure 14. SEM micrograph showing fracture of both iron and copper intermetallics in alloy B319.2 (0.8% Fe, DAS 23 μm, unmodified).

Figure 14 shows the fractograph taken from the unmodified B319.2 alloy sample containing 0.8% Fe, obtained at the highest cooling rate. Transgranular fracture of all intermetallics viz., the α-Fe, β-Fe, and Cu-containing phases is observed. In this alloy, containing a higher level of Mg, the Cu-phase would include $Al_5Mg_8Cu_2Si_6$ and $Al_{15}(Mn,Fe,Cu)_3Si_2$, in addition to the $CuAl_2$ phase. The presence of cracked Si particles and associated microvoids are also seen.

A comparison with the fractograph shown in **Figure 6** (same Fe level, but lowest cooling rate) shows how a high cooling rate is more effective than the Fe content in determining the size of the β-platelets that result and, hence, the nature of the fracture, i.e., fragmentation or cleavage (this point is further brought out in the context of **Figure 16**). The corresponding E_I, E_P, and E_T values of this sample are 6.18, 1.40, and 7.58 J, respectively. However, as **Figure 15** shows, the β-platelet can still fracture by cleavage, particularly in regions where several platelets have precipitated together. The smooth surface of the various β layers in the figure clearly indicate that fracture in this part of the specimen occurred by cleavage. It is not hard to imagine the branched appearance of these several platelets in a two-dimensional optical micrograph.
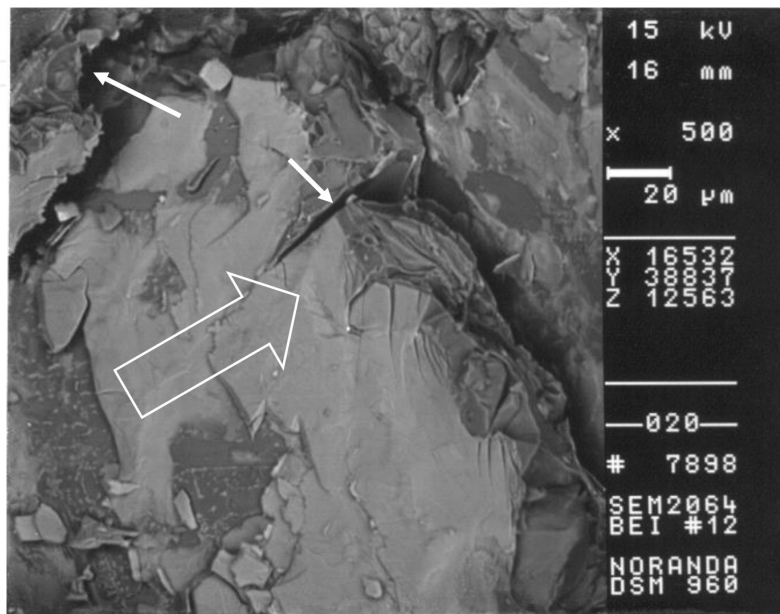

Figure 15. SEM micrograph showing fracture of β-platelets in alloy B319.2 (0.8% Fe, DAS 23 μm, unmodified).

The SEM fractograph, shown in **Figure 16**, of the same 0.8% Fe-containing unmodified B319.2 alloy obtained, however, at the lowest cooling rate shows clearly the massive dimensions that the β-Al_5FeSi platelets can attain at the same 0.8% Fe level, depending upon the solidification conditions. Again, the platelet fractures by cleavage, the open arrow indicating the cleavage direction. Secondary cracks (white arrows) are also observed when the crack propagates through the eutectic Si regions.

Figures 17 and **18** are SEM fractographs obtained from modified 319.2 and B319.2 alloys, respectively, under the same Fe and solidification conditions (0.8% Fe, lowest cooling rate). The rather large dimensions of the pore observed in **Figure 17**, as evidenced by the untouched α-Al dendrites sitting inside, show how the β-phase platelets lodged beside (1) and between

(2) the dendrites restrict the flow of the liquid metal in the surrounding region and hence lead to the formation of porosity. The presence of the pore facilitates fracture. In contrast to the fractured β-platelets (e.g., 3 and 4) around the pore area, the β-platelets within the pore did not participate in the fracture process and remained quite intact.

Figure 16. SEM micrograph showing fracture of β-AlFeSi intermetallics in alloy B319.2 (0.8% Fe, DAS 83 μm, unmodified).

Figure 17. SEM micrograph showing the effect of porosity participating in the fracture behavior of alloy 319.2 (0.8% Fe, DAS 83 μm, modified).
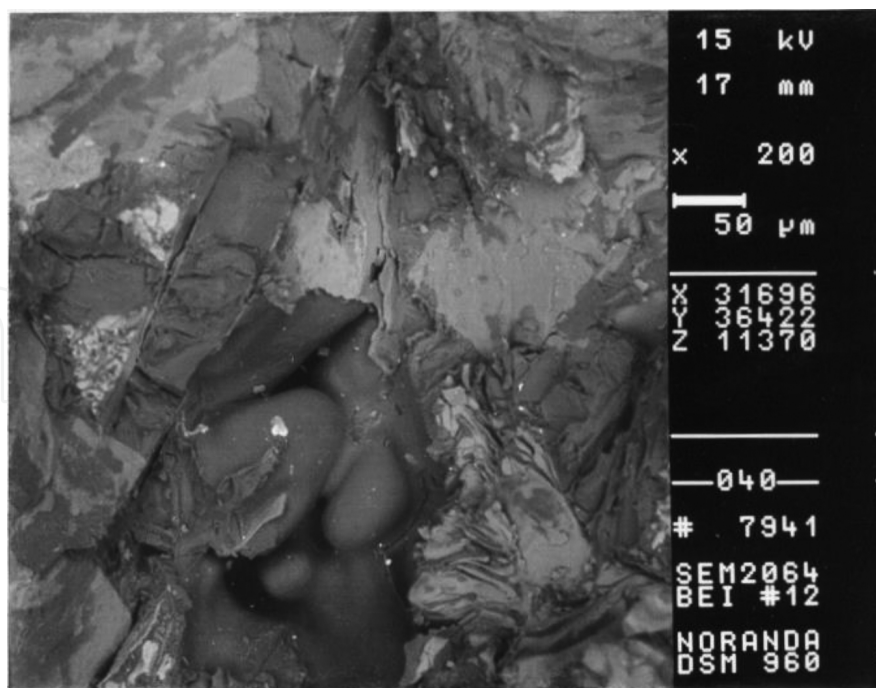
Figure 18. SEM micrograph showing the effect of porosity participating in the fracture of alloy B319.2 (0.8% Fe, DAS 83 μm, unmodified).

Similarly, **Figure 18** shows an example of a pore observed on the fracture surface of the modified B319.2 alloy. In this instance, the pore appears to be much smaller in dimension and more shallow than the one depicted in **Figure 17** with fragments of cleaved β-phase platelets on the surrounding fracture surface. The dissolution of the β-platelets due to the effect of Sr is more evident in this fractograph.
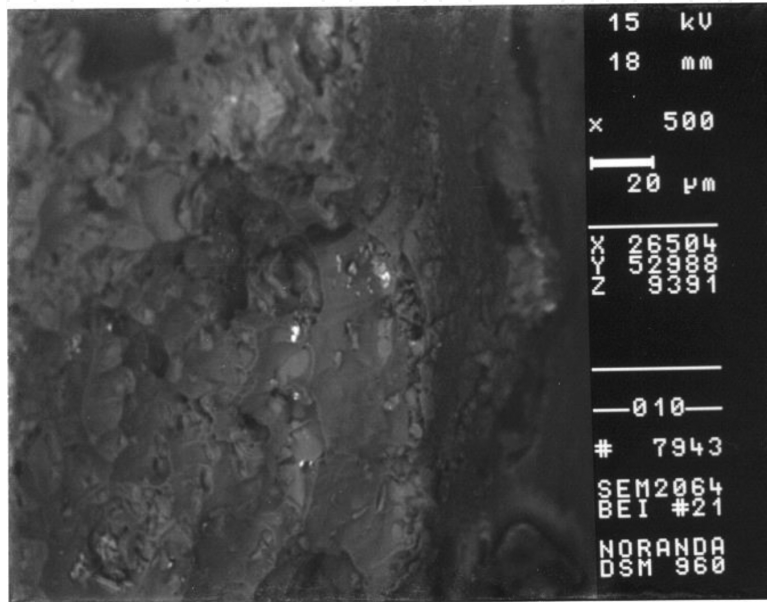
3.3. Alloy A356.2 (alloy C)

As was done for the 319 alloys, the fractographs of A356.2 alloy samples covering the lowest Fe content—highest cooling rate/optimum property and highest Fe content—lowest cooling rate/minimum property conditions have been selected for discussion purposes, to bring out the contrast in their fracture modes and hence comprehend the difference in their impact properties.

As Voigt and Bye [35] have commented, features appearing on the fracture surfaces of Al-Si-Mg casting alloys such as A356 alloys can be very difficult to interpret due to the lack of SEM contrast between the α-Al and the eutectic Si phases appearing on the surface. As Al and Si are close in their atomic numbers, even the use of SEM techniques such as backscattered electron imaging cannot provide additional phase contrast. However, the features observed on the fracture surfaces of A356 alloys can be more clearly interpreted based on a study of the surface crack initiation and propagation process. Usually, by observing the microstructure just below the surface that can be observed inside the crack using SEM techniques, or else by studying longitudinal sections of the fractured samples (perpendicular to the fracture surface)

using optical microscopy, additional information can be obtained that is useful in analyzing the fracture behavior.

Figures 19 and **20** are the SEM fractographs taken from the modified A356.2 alloy sample containing 0.1% Fe and obtained at the highest cooling rate. **Figure 19** shows the fracture to be of the transgranular dimpled rupture type. As mentioned before, the BEI image does not provide a good phase contrast.

Figure 19. SEM micrograph showing fracture surface of alloy A356.2 (0.1% Fe, DAS 23 μm, modified, edge).
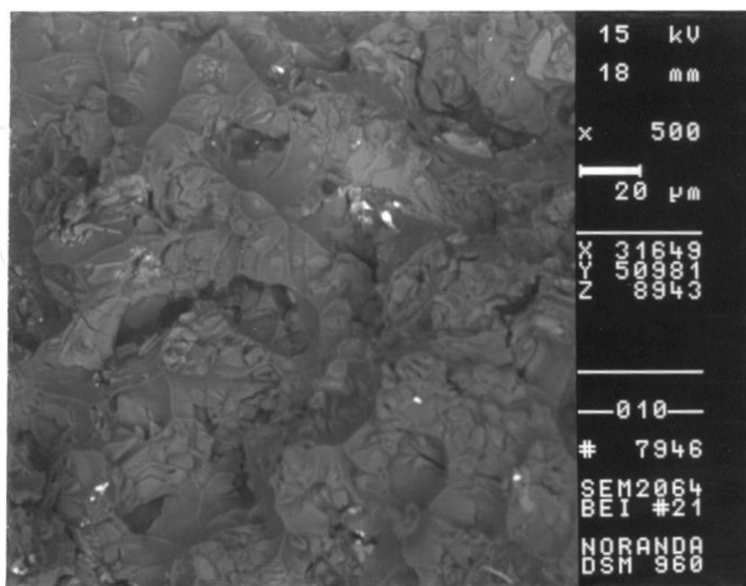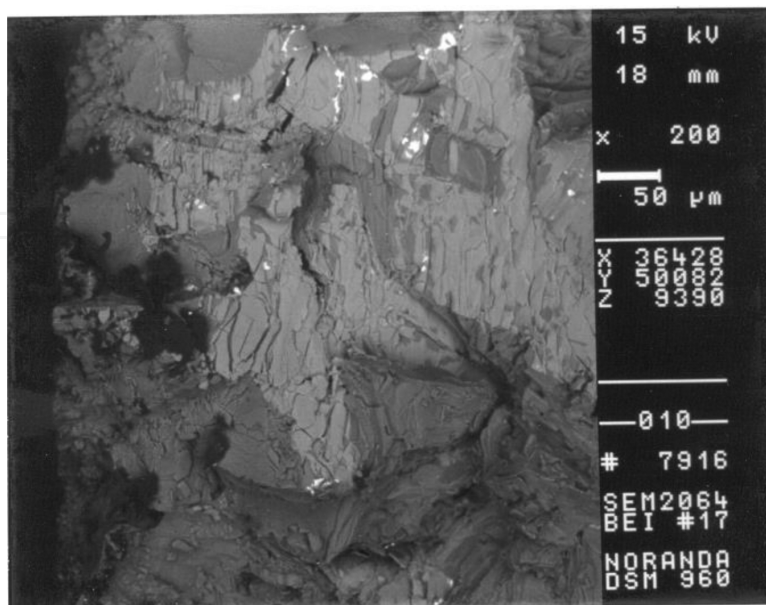

Figure 20. SEM micrograph showing fracture surface of alloy A356.2 (0.1% Fe, DAS 23 μm, modified, center).

The fractograph of **Figure 20** taken from the center of the sample shows these features more clearly. Note the fine Si particles in the structure. The absence of intermetallics, due to the low Fe content, together with the fine Si particles obtained under the optimum alloy conditions of a high cooling rate and Sr modification, results in the sample exhibiting the highest impact energy (80.88 J).

Figures 21 and **22** depict the SEM fractographs of the unmodified A356.2 alloy sample containing a high Fe level (0.6%) and obtained at the lowest cooling rate. The presence of massive β-Al_5FeSi platelets in the alloy microstructure under these conditions results in the brittle fracture of the sample. As **Figure 21** shows, crack initiation takes place by the fragmentation of the β-phase at the edge of the sample and some amount of transgranular fracture, as well, whereas the crack propagates by cleavage fracture, as evidenced by the relatively smooth surfaces of the β-platelets observed in **Figure 22**, as also by intergranular fracture. Accordingly, the impact energy of this sample was 2.45 J.

When the same alloy is modified, crack initiation occurs by fragmentation of the β-Al_5FeSi platelet, followed by cleavage, as seen in **Figure 23**. Modified silicon eutectic regions around the β-platelet can also be distinguished. **Figure 24** shows that the fracture mode is a mixture of cleavage and intergranular fracture.

The high magnification SEM fractograph of an unmodified A356.2 alloy sample containing 0.1% Fe and obtained at the lowest cooling rate, **Figure 25**, reveals the eutectic Si regions much more clearly, where the fracture is seen to occur by the transgranular brittle fracture of the acicular Si particles (see circled areas).

Figure 21. SEM micrograph showing the role of β-Al_5FeSi intermetallics in initiating fracture in alloy A356.2 (0.6% Fe, DAS 75μm, unmodified).
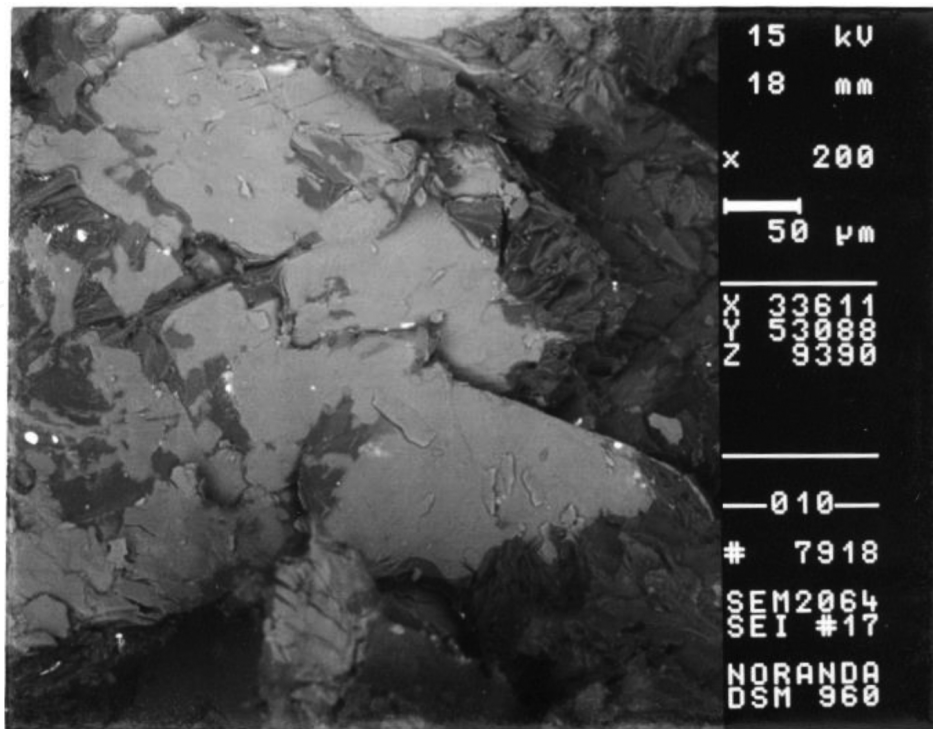
Figure 22. SEM micrograph showing crack propagation in alloy A356.2 (0.6% Fe, DAS 75 μm, unmodified).
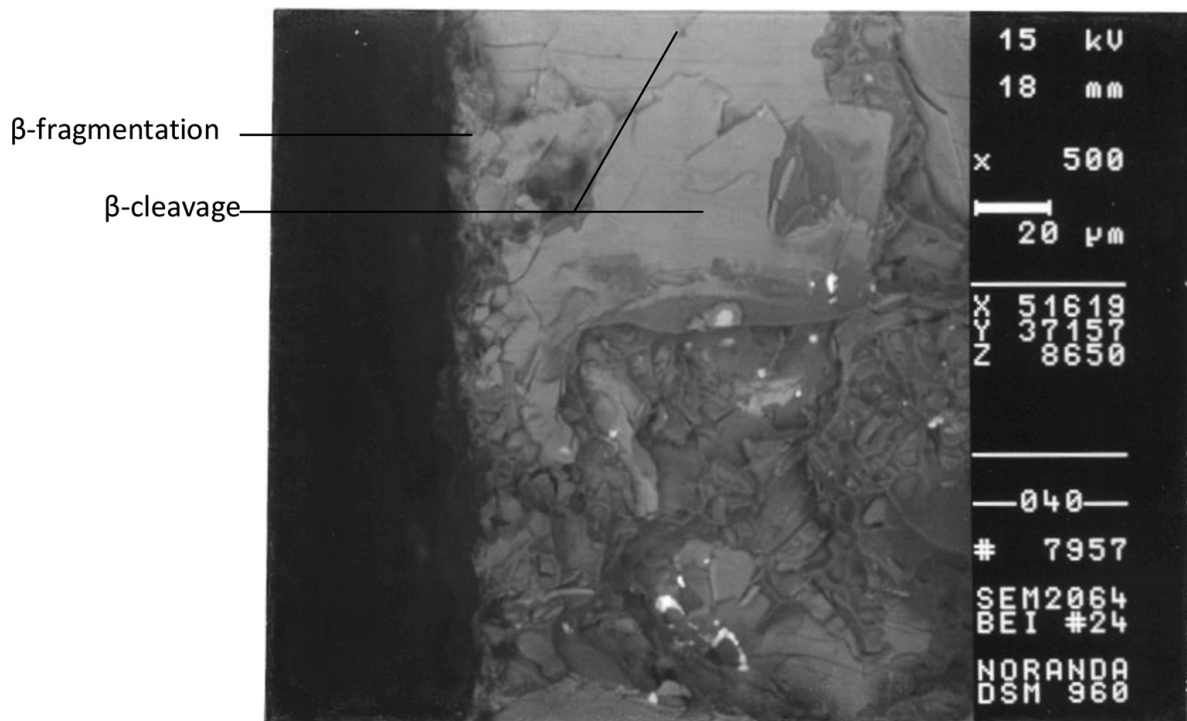

Figure 23. SEM micrograph showing fracture surface of alloy A356.2 (0.6% Fe, DAS 75 μm, modified, edge).
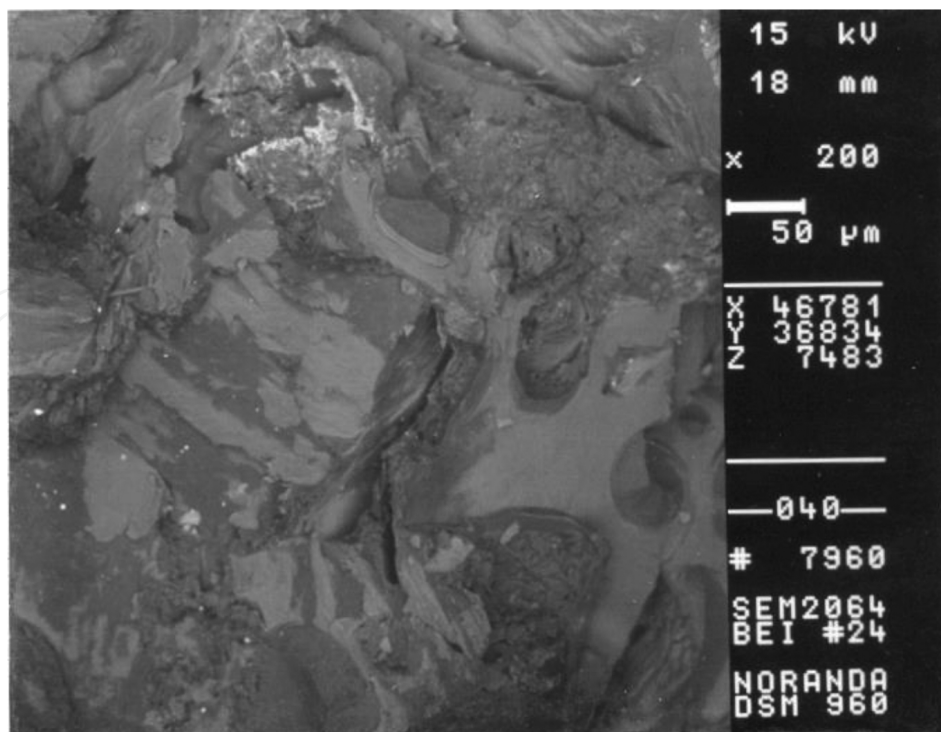
Figure 24. SEM micrograph showing fracture surface of alloy A356.2 (0.6% Fe, DAS 75 μm, modified, center).
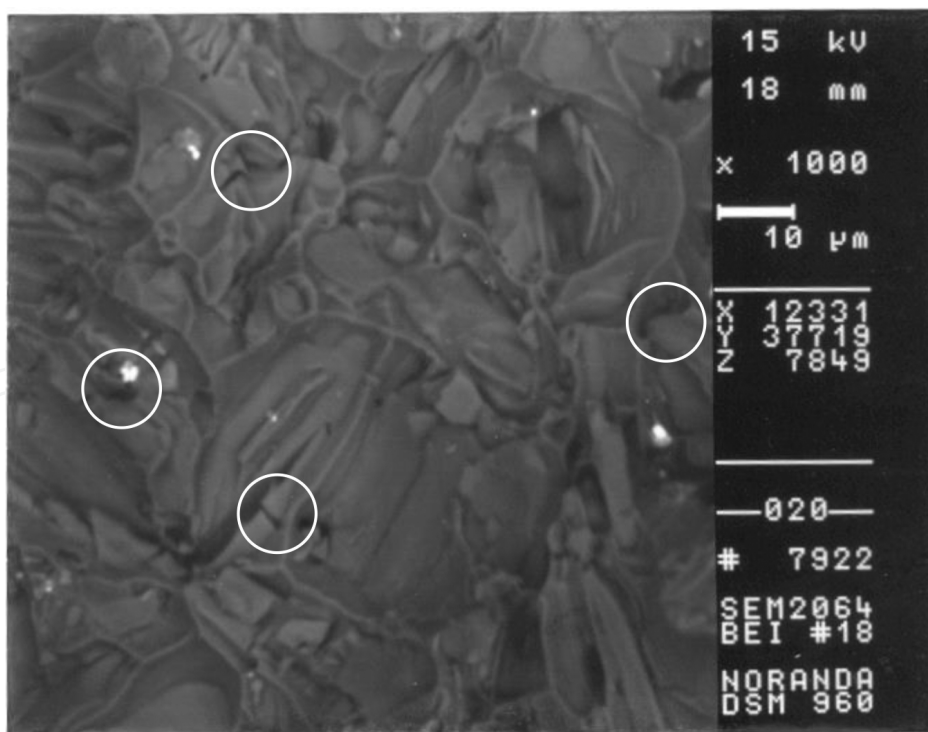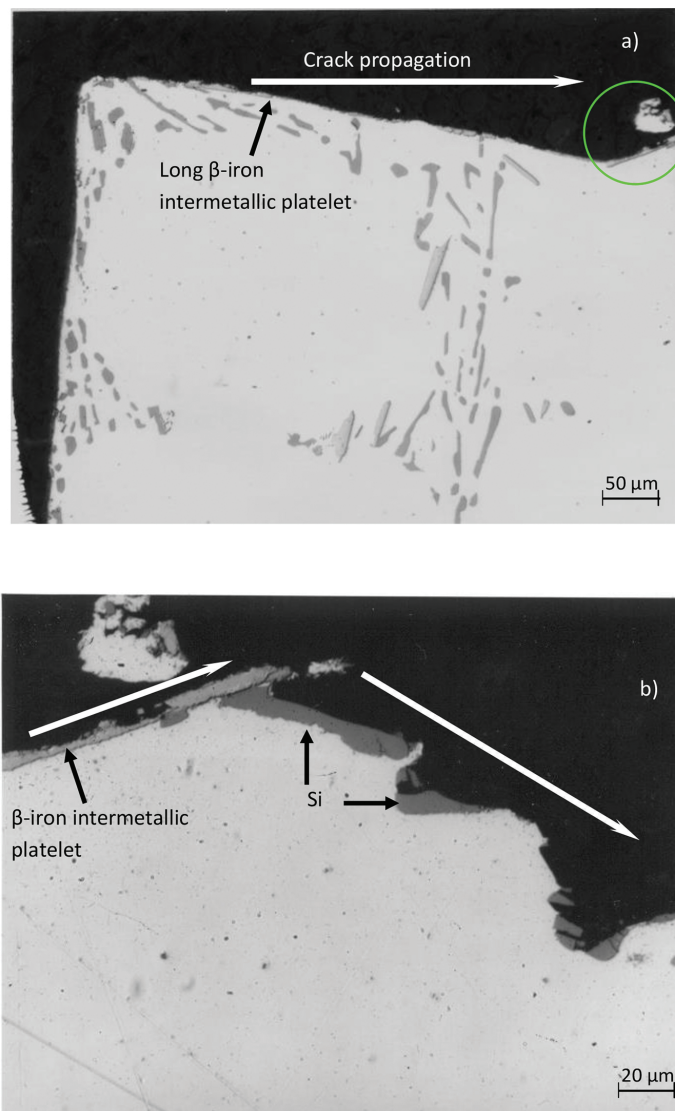

Figure 25. SEM micrograph showing fracture of eutectic Si particles in alloy A356.2 (0.1% Fe, DAS 75 μm, unmodified).

3.4. Optical microscope fractography

Regardless of SEM fractography, it is also quite useful to examine the fracture profile on sections perpendicular to the fracture surface. This can be carried out easily using an optical microscope. In this way, the origin of the fracture can be examined to determine if important microstructural abnormalities are present that either caused or contributed to fracture initiation. It is also possible to determine if the fracture path at the initiation site is transgranular or intergranular and to determine if the fracture path is specific to any phase or constituent present [36]. Some examples of the longitudinal sections of the A356.2 alloy samples are presented in this section with a view to further clarify the fracture process in these samples as their SEM fractographs did not display as good a phase contrast as those shown by the 319 alloy samples.

Figure 26. Optical micrographs showing fracture behavior of alloy A356.2 (0.6% Fe, DAS 75µm, unmodified, edge). A high magnification micrograph of the circled area in (a) is shown in (b).
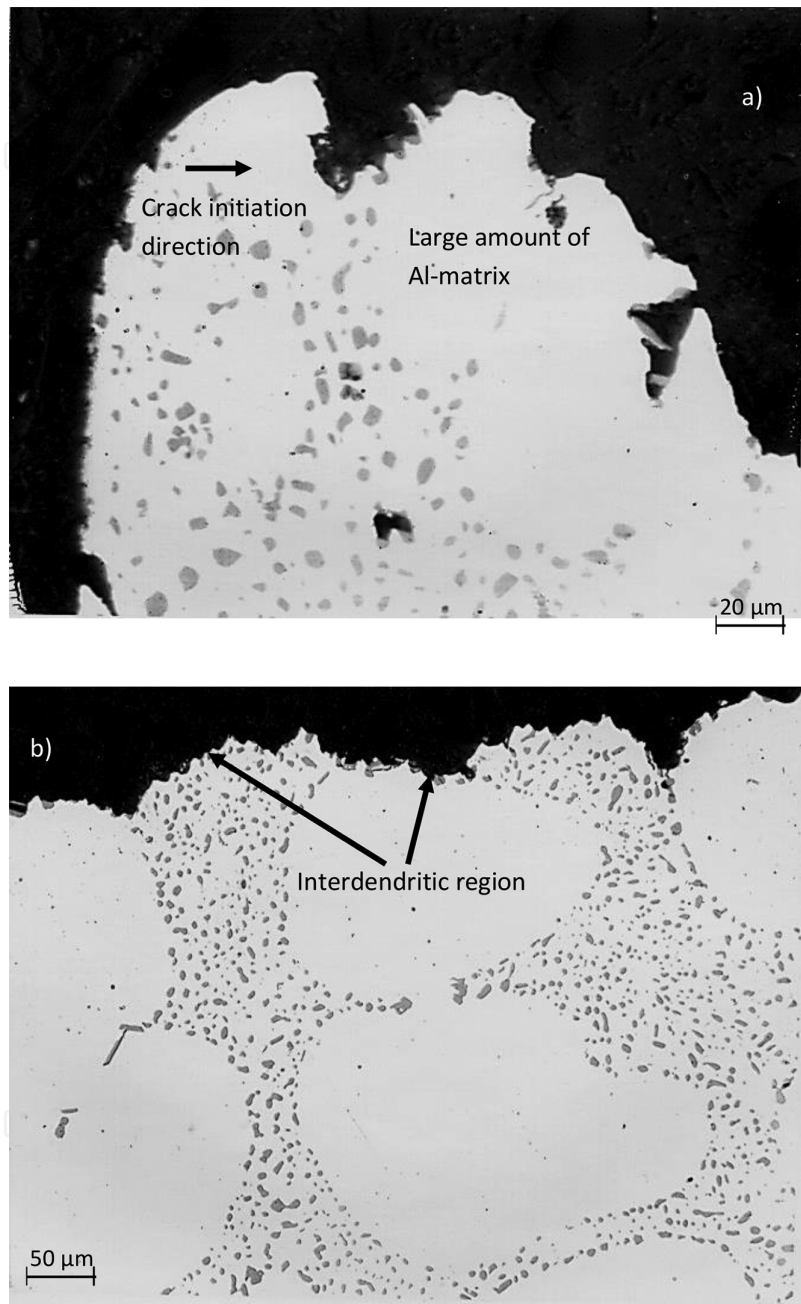
The optical micrographs presented in **Figure 26** show the polished longitudinal section of the fractured A356.2 unmodified alloy sample containing 0.6% Fe, obtained at the lowest cooling rate. In **Figure 26(a)**, the edge of the sample on the left shows how crack initiation occurs by cleavage and/or transgranular fracture of the Si particles and β-Al$_5$FeSi platelets. The sample edge corner is relatively straight, indicating that cracking occurred almost immediately, i.e., by brittle fracture mode, and the crack propagated along the direction shown.
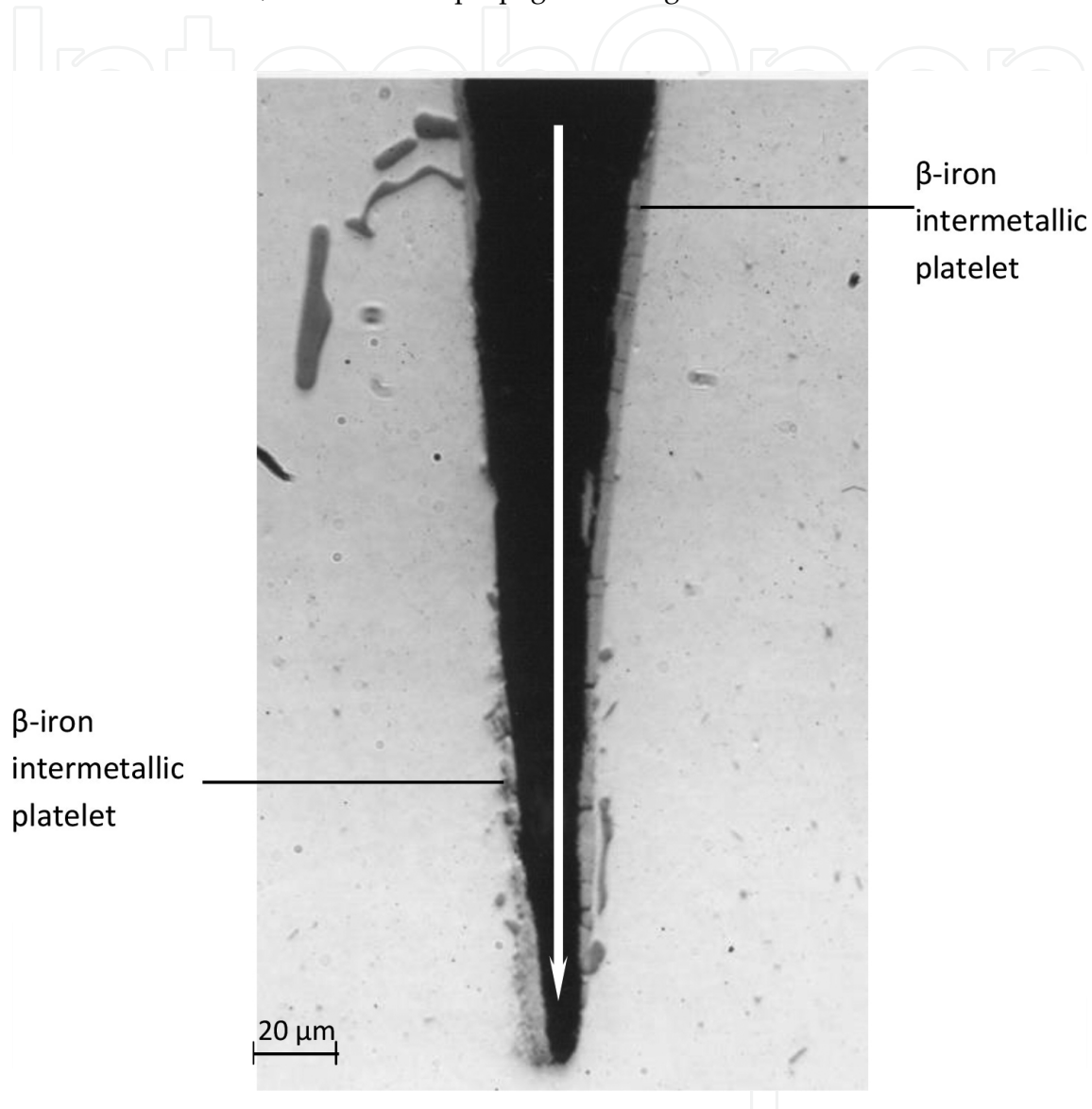
Figure 27. Optical micrograph showing fracture behavior of alloy A356.2 (0.4% Fe, DAS 23 μm, unmodified, edge, 500×).

A higher magnification micrograph, **Figure 26(b)**, of the fracture surface corresponding to the circled area in **Figure 26(a)** shows how the crack propagates further along the fracture surface by cleavage of the β-iron intermetallic and coarse Si particles. The persistence of such coarse Si particles, even after solution heat treatment at 540°C/8 h, aids in inducing the brittle fracture of the sample. Correspondingly, under such alloy conditions, the sample exhibited the lowest impact energy (2.45 J). **Figure 26** provides a good example of how optical microscopy can aid

in providing a clearer interpretation of the crack initiation and propagation in A356 type Al-Si-Mg alloys.

Figure 28. Optical micrographs showing fracture behavior of alloy A356.2 (0.1% Fe, DAS 23 μm, Sr-modified, edge).

The optical micrograph in **Figure 27**, taken from an A356.2 unmodified alloy sample containing 0.4% Fe and obtained at the highest cooling rate, shows the propagation of a secondary crack (see white arrow) that splits a β-Al_5FeSi platelet right through the middle. The crack propagates to the end of the platelet, till it reaches the aluminum matrix which, being ductile, allows for stress relaxation at the crack tip by local plastic flow.

Compared to the micrographs shown in **Figure 26**, those obtained from the A356.2 alloy sample corresponding to optimum energy conditions (viz., 0.1% Fe, lowest cooling rate, Sr-modified alloy), **Figure 28(a)** shows how the sample edge is more curved or rounded , rather than flat as was observed in the case of the unmodified alloy sample of **Figure 26**. The curvature of the fracture surface, also clearly observed in **Figure 28(b)**, indicates a ductile mode of rupture as the crack propagates through the well-modified Si eutectic regions. The E_I, E_P, and E_T values in this case are 60.44, 20.44, and 80.88 J, respectively, compared to 1.41. 1.31, and 2.45 J in the case of the sample shown in **Figure 26**.
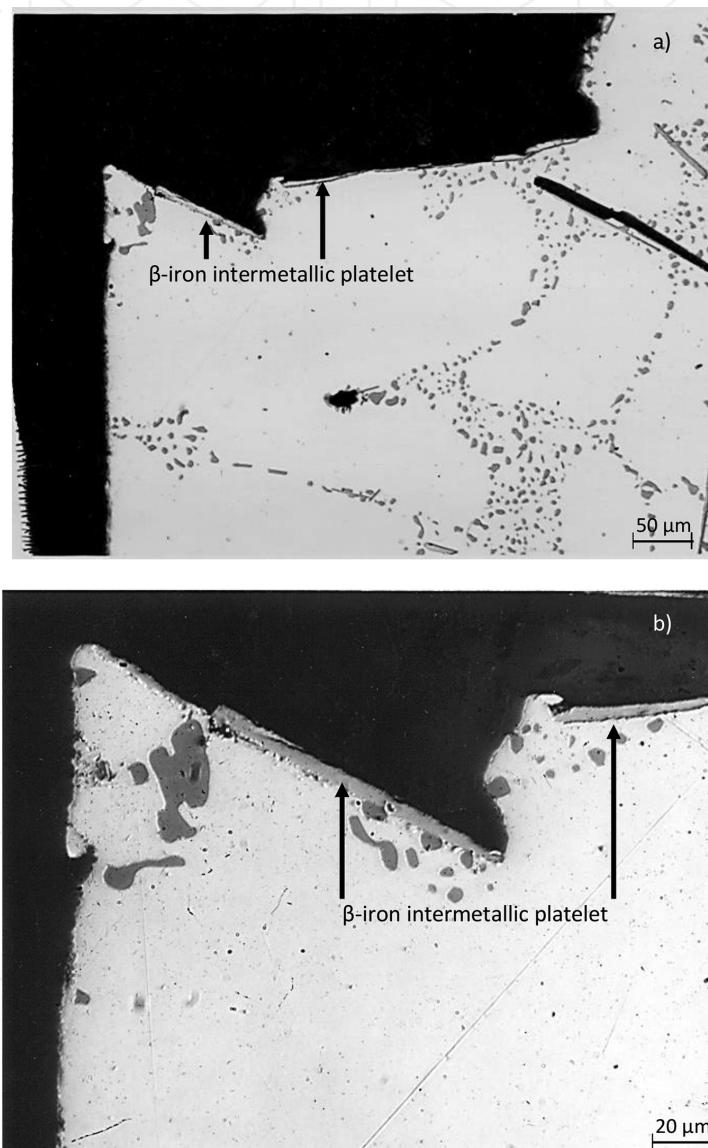
Figure 29. Optical micrographs showing fracture behavior of alloy A356.2 (0.6% Fe, DAS 75 µm, Sr-modified, edge).

However, when the alloy Fe level is increased and the cooling rate decreased to its lowest value, even in the Sr-modified alloy, the fracture still occurs mainly by cleavage of the brittle β-Al$_5$FeSi platelets, as seen in **Figure 29(a)**. Note the sharp edge of the sample fracture surface in this

case, compared to **Figure 28**. **Figure 29(b)** shows these features much more clearly at a high magnification. In instances when the crack propagates through the more ductile Al-Si regions, the fracture surface is more rounded than sharp. The corresponding E_I, E_P, and E_T values are 3.41, 1.46, and 4.87 J, respectively.

4. Conclusions

The present research was carried out on two of the main alloys used in automotive applications, namely 319 and 356 alloys, where the effects of iron content, Sr modification, and cooling rate on the impact properties were studied. The main observations on the fracture behavior in relation to the impact properties are presented in this chapter and may be summarized as follows.

1. At low iron levels and high cooling rates (0.4% Fe, 23 μm DAS), and in the unmodified condition, 319 alloys undergo crack initiation through the fragmentation of Si particles, β-iron intermetallics, and $CuAl_2$ particles. Crack propagation takes place through the linking of the fragmented particles. A dimpled structure is observed for the Sr-modified alloys, indicating ductile fracture.

2. At high iron levels and low cooling rates (0.8% Fe, 83 μm DAS), in the unmodified condition, crack initiation and propagation occur through the cleavage of β-Al_5FeSi platelets (rather than by decohesion of the β-iron platelets from the matrix).

3. The morphology of the β-iron intermetallic platelets (individual or branched) is important in determining the direction of crack propagation. Cracks also propagate through the fracture of undissolved $CuAl_2$ or other Cu-intermetallics such as Al_7Cu_2Fe, as well as through fragmented Si particles. In the Sr-modified alloys, cracks are initiated mostly with the fragmentation or cleavage of perforated β-phase platelets.

4. A small amount of crack initiation can also take place through the fragmentation of coarse Si particles that have not fully undergone spheroidization or undissolved Cu-intermetallics. Thus, all microstructural constituents contribute to the fracture process.

5. In the A356.2 alloys, in samples obtained under optimum conditions (0.1% Fe, 23 μm DAS, Sr-modified alloy), cracks initiate mainly through the fracture of Si particles or the debonding of the Si particles from the Al matrix.

6. In the unmodified condition, cracks mainly propagate through the coalescence of fractured Si particles, except where β-iron intermetallics are present, in which case the latter takes priority in fracture propagation.

7. In the Sr-modified condition, more of the Al matrix is involved when cracks propagate through the linkage of fractured/debonded Si particles, as well as fragmented β-iron intermetallics. For samples characterized by low-impact energies, crack initiation and propagation occurs mainly through the cleavage of β-iron intermetallics.

Acknowledgements

Author details

Zheyuan Ma[1], Agnes M. Samuel[1], Herbert W. Doty[2] and Fawzy H. Samuel[1*]

*Address all correspondence to: fhsamuel@uqac.ca

1 University of Québec at Chicoutimi, Québec, Canada

2 Materials Technology, Pontiac, MI, USA

References

[1]   Gabriel BL. SEM: A User's Manual for Materials Science. Metals Park, OH: American Society for Metals; 1985, p. 97.

[2]   Gerberich WW. Microstructure and Fracture. In: Metals Handbook, Vol.8: Mechanical Testing. 9th ed. Metals Park, OH: American Society for Metals; 1985, p. 476–491. ASM Handbook Committee. John R. Newby, Coordinator.

[3]   Ma Z, Samuel AM, Doty HW, Valtierra S, Samuel FH. Effect of Fe content on the fracture behaviour of Al–Si–Cu cast alloys. Materials & Design. 2014;57:366–373.

[4]   Kerlins V, Phillips A. Modes of Fracture. In: Metals Handbook, Vol. 12: Fractography. 9th ed. Metals Park, OH: American Society for Metals; 1987, p. 12–71. ASM Handbook Committee. The Editors.

[5]   Wang QG, Cáceres CH. The fracture mode in Al–Si–Mg casting alloys. Materials Science and Engineering A. 1998;241:72–82.

[6]   Ammar HR, Samuel AM, Samuel FH, Simielli E, Sigworth GK, Lin JC. Influence of aging parameters on the tensile properties and quality index of Al-9 Pct Si-1.8 Pct Cu-0.5 Pct Mg 354-type casting alloys. Metallurgical and Materials Transactions A. 2012;43(1):61–73.

[7]   Gall K, Yang N, Horstemeyer M, McDowell DL, Fan J. The debonding and fracture of Si particles during the fatigue of a cast Al-Si alloy. Metallurgical and Materials Transactions A. 1990;30A(12):3079–3088.

[8] Hafiz MF, Kobayashi T. A study on the microstructure-fracture behavior relations in Al-Si casting alloys. Scripta Metallurgica et Materialia. 1994;30:475–480.

[9] Lee FT, Major JF, Samuel FH. Effect of silicon particles on the fatigue growth characteristics of Al-12 wt pct Si-0.35 wt pct Mg-(0 to 0.02) wt pct Sr casting alloys. Metallurgical and Materials Transactions A. 1995;26:1553–1570.

[10] Li Z, Samuel AM, Samuel FH, Ravindran C, Doty HW, Valtierra S. Parameters controlling the performance of AA319-type alloys Part II. Impact properties and fractography. Materials Science and Engineering A. 2004;367:111–122.

[11] Brooks CR, Choudhury A. Metallurgical Failure Analysis. New York: McGraw-Hill Inc.; 1993.

[12] Tiryakiolu M. Fracture toughness potential of cast Al-7% Si-Mg alloys. Materials Science and Engineering A. 2008;497:512–514.

[13] Elsebaie O, Samuel AM, Samuel FH, Doty HW. Impact toughness of Al–Si–Cu–Mg–Fe cast alloys: effects of minor additives and aging conditions. Materials & Design. 2014;60:496–509.

[14] Elsebaie O, Mohamed AMA, Samuel AM, Samuel FH, Al-Ahmari AMA. The role of alloying additives and aging treatment on the impact behavior of 319 cast alloy. Materials and Design. 2011;32:3205–3220.

[15] Hafiz MF, Kobayashi T, Fat-Halla N. Role of microstructure in relation to the toughness of hypoeutectic Al–Si casting alloy. Cast Metals. 1990;7:103–111.

[16] Lados DA, Apelian D, Major JF. Fatigue crack growth mechanisms at the microstructure scale in Al-Si-Mg cast alloys: mechanisms in regions II and III. Metallurgical and Materials Transactions A. 2006;37A:2405–2418.

[17] Samuel AM, Doty HW, Valtierra S, Samuel FH. Relationship between tensile and impact properties in Al–Si–Cu–Mg cast alloys and their fracture mechanisms. Materials & Design. 2014;53:938–946.

[18] Mrówka-Nowotnik G. The effect of intermetallics on the fracture mechanism in AlSi1MgMn alloy. Journal of Achievements in Materials and Manufacturing Engineering. 2008;30:1–8.

[19] Mrówka-Nowotnik G, Sieniawski J, Nowotnik A. Tensile properties and fracture toughness of heat treated 6082 alloy. Journal of Achievements in Materials and Manufacturing Engineering. 2006;17:105–108.

[20] Horng JH, Jiang DS, Lui TS, Chen LH. The fracture behaviour of A356 alloys with different iron contents under resonant vibration. International Journal of Cast Metals Research. 2000;13:215–222.

[21] Taylor JA. Iron-containing intermetallic phases in Al-Si based casting alloys. Procedia Materials Science. 2012;1:19–33.

[22] Dinnis CM, Taylor JA. Manganese as a "neutraliser" of iron-related porosity in Al-Si foundry alloys. In: Jones H, editor, Proceedings of the 5th Decennial Conference on Solidification Processing (SP07), 23–25 July 2007; Sheffield, UK: Maney; 2007, p. 566–570.

[23] Villeneuve C, Samuel AM, Samuel FH, Doty HW, Valtierra S. Role of trace elements in enhancing the performance of 319 aluminum foundry alloys. AFS Transactions. 2001;109:1–14.

[24] Al Kahtani SA, Doty HW, Samuel FH. Combined effect of melt thermal treatment and solution heat treatment on eutectic Si particles in cast Al-Si alloys. International Journal of Cast Metals Research. 2014;27:38–48.

[25] Câceres CH, Davidson CJ, Griffiths JR. The deformation and fracture behavior of an Al-Si-Mg casting alloy. Materials Science and Engineering A. 1995;197:171–179.

[26] Wang QG, Câceres CH, Griffiths JR. Transgranular and Intergranular Fracture in Al-Si-Mg Casting Alloys. In: Karihaloo BL, Mai YW, Ripley MI, editors, Advances in Fracture Research: Proceedings of the Ninth International Conference on Fracture (ICF9), 1–5 April 1997; Sydney, Australia, , 5:2511–2518.

[27] Samuel AM, Samuel FH. A metallographic study of porosity and fracture behavior in relation to tensile properties in 319.2 end chill castings. Metallurgical and Materials Transactions A. 1995;26A:2539–2372.

[28] Dinnis CM, Taylor JA, Dahle AK. Iron-related porosity in Al–Si–(Cu) foundry alloys. Materials Science and Engineering A. 2006;425:286–296.

[29] Estensoro FJ, Pelayo A, Insarri AM. Fatigue Behavior of Two Cast Aluminum-Silicon Alloys. In: Proceedings of European Conference on Fracture – Mechanisms and Mechanics of Damage and Failure of Engineering Materials and Structures (ECF 11), 3–6 September 1996; Poitiers, Futuroscope, France, p. 1045–1050.

[30] Lados DA, Apelian D. The effect of residual stress on the fatigue crack growth behavior of Al-Si-Mg cast alloys – mechanisms and corrective mathematical models. Metallurgical and Materials Transactions A. 2006;37:133–145.

[31] Savelli S, Buffière J-Y, Fougères R. Pore characterization in a model cast aluminum alloy and its quantitative relation to fatigue life studied by synchrotron X-ray microtomography. Materials Science Forum. 2000;331–337:197–202.

[32] The ASM Committee on Fractography by Electron Microscopy. The Scanning Electron Microscope and Its Application to Fractography. In: Metals Handbook, Vol. 9: Fractography and Atlas Fractographs. 8th ed. Metals Park, OH: American Society for Metals; 1978. p. 49–53.

[33] Li Z, Samuel AM, Samuel FH, Ravindran C, Valtierra S, Doty HW. Parameters controlling the performance of AA319-type alloys Part I. Tensile properties. Materials Science and Engineering A. 2004;367:96–110.

[34] Mohamed AMA, Samuel FH. A Review on the Heat Treatment of Al-Si-Cu/Mg Casting Alloys. In: F. Czerwinski, editor. Heat Treatment: Conventional and Novel Applications. InTech; 2012, Rijeka, Croatia. Chapter 4. DOI: 10.5772/2798.

[35] Voigt RC, Bye DR. Microstructural aspects of fracture in A356. AFS Transactions. 1991;99:33–50.

[36] Van der Voort GF. Visual Examination and Light Microscopy. In: Metals Handbook, Vol. 12: Fractography, 9th ed. Metals Park, OH: American Society for Metals; 1987. p. 91–165. ASM Handbook Committee. The Editors.